

Modeling of stationary waves on a thin viscous film down an inclined plane at high Reynolds numbers and moderate Weber numbers using energy integral method

R. Usha and B. Uma

Department of Mathematics, Indian Institute of Technology, Madras, Chennai 600 036, India

(Received 27 December 2002; accepted 6 April 2004; published online 4 June 2004)

The theory describing the nonlinear stationary waves of finite amplitude and long wavelength on a thin viscous Newtonian film at high Reynolds numbers and moderate Weber numbers has been developed using the energy integral method (EIM). The linear instability of the uniform flow by EIM has been analyzed and the linear instability threshold has been obtained as $\cot \theta/Re=6/5$, which agrees with the classical results of the Orr–Sommerfeld analysis by Benjamin [J. Fluid Mech. **2**, 554 (1957)] and Yih [Phys. Fluids **6**, 321 (1963)] and verified experimentally by Liu and Gollub [Phys. Rev. Lett. **70**, 2289 (1993)]. Further, in the frame of reference moving with the steady wave speed, the second order approximate equations reduce to a third order dynamical system. While wave transitions in real life involve complex spatio-temporal dynamics and many of these transitions lead to chaotic waves that are not stationary traveling waves, bifurcation of stationary traveling waves has been examined as a preliminary study of the more complex transitions. Stability of the fixed points of the dynamical system, parametric regimes of heteroclinic orbits and Hopf bifurcations are delineated. Numerical integration has been carried out in order to study the different bifurcation scenarios as the phase speed deviates from the Hopf-bifurcation thresholds. Four different bifurcation scenarios have been observed and the dependence of bifurcation scenarios on the inclination angle, Reynolds numbers and Weber numbers have been discussed. Although the results obtained by the momentum integral method and EIM exhibit similar bifurcation scenarios, there are quantitative differences which shows that the modeling differences exist in the literature. © 2004 American Institute of Physics. [DOI: 10.1063/1.1755704]

I. INTRODUCTION

The hydrodynamic behavior of a thin wavy liquid film down an inclined plane or a vertical wall has attracted the attention of several investigators due to the necessity for accurate modeling of a variety of dynamical phenomena exhibited by the wavy liquid film and its many applications in industry. Since the pioneering work by Kapitza,¹ who characterized the types of wave structures seen on an initially flat film, several investigations have been carried out and these provide a theoretical description of the wave evolution process on a liquid film flowing down an inclined surface or a vertical wall. Benney's² long-wave model has considered the evolution of finite-amplitude disturbances to the flat film. The single nonlinear partial differential equation for the evolution of the free surface to which the governing equations are reduced, show that solitary and shock-like film profiles are its possible solutions, when the partial differential equation is valid up to a particular order in ϵ (the ratio of the thickness of the flat film to the wave length of the disturbance in the flow direction). His analysis has not predicted the existence of finite-amplitude traveling waves near the onset of the instability and this failure has been attributed to his scaling [Weber number, $We \sim O(1)$ and Reynolds number, $Re \sim O(1)$] which has surface tension left out from the governing equations. Following this analysis, there have

been several reports towards the investigation of the long-wave surface evolution equation developed to various orders of either $We \sim O(1)$ or $\epsilon^2 We \sim O(1)$.^{3–11}

Several models based on a boundary layer type of analysis have been developed^{12–19} and the solutions of the resulting surface evolution equations have predicted the nonlinear dynamics of the film at finite values of Reynolds number. This integral boundary layer method uses a self-similar velocity profile assumption to derive a two-equation model to describe the dynamics of moderate to large amplitude disturbances. The advantages of the integral method are that the model equations (i) are valid up to a larger range of Reynolds numbers, (ii) are simple and it is possible to obtain analytical solutions, (iii) provide a means for a comparison of different models and boundary conditions, and (iv) have solutions which help in the determination of flow parameters. It is important to note that the integral approach has been quite effective and popular in the study of flow and stability characteristics of wavy films in spite of the increasing advantage provided by the powerful computers and efficient numerical methods.²⁰

Most of the above investigations using the integral boundary layer method employ the momentum integral approach which is based on the fact that the introduction of fluid inertia in a thin film does not appreciably alter the velocity profile within the film. The fundamental approxima-

tion is that the velocity field with fluid inertia remains exactly the same as in uniform parallel primary flow. In the momentum approximation, the velocity profiles for the uniform flow are introduced into the boundary layer approximations of the governing equations and the equations are integrated across the film to provide a two equation model describing the dynamics of the waves. It is worth mentioning here that, apart from the above investigations on the flow and stability characteristics of Newtonian wavy films in which the integral method has been used, the integral formulation has been very effectively used in the study of hydrodynamics of gravity driven film flows of non-Newtonian thin films.^{21–25} The predictions by this approach agree well with the experimental data for the developing flow in the hydrodynamic entrance region.^{26–28}

Although the momentum integral approach has been extensively employed, the energy integral approximation has not been applied in the analysis of flow system and stability characteristics of thin film flow down an inclined or a vertical wall. In the energy approximation, the governing momentum equation is premultiplied by the flow velocity (making each term represent power per unit volume). The velocity profiles for the uniform parallel primary flow are then introduced and each term is integrated across the film to provide a two equation model describing the evolution of the free surface.

In their study on squeeze-film damper flows, Crandall and El-Shafei²⁹ have shown that the energy integral method's (EIM) predictions agree with the exact solutions to first order in the Reynolds number and that the error in the first order terms of the momentum approximation is 20% at low Reynolds numbers. They have pointed out that the energy integral formulation is superior to momentum integral method in the determination of the effects of inertia on squeeze-film damper performance. Elkouh³⁰ has pointed out that the EIM has led to a more accurate determination of the pressure distribution for the steady flow in a hydrostatic thrust bearing. Also, Elkouh³¹ has shown that the expression for the pressure distribution obtained for Newtonian circular squeeze film using EIM is identical to that obtained by an iteration technique by Kuzma³² which has been observed to be in good agreement with the available experimental results. Further, the investigations by Kapur and Verma³³ on magneto-hydrodynamic thrust bearings, by Turns³⁴ on flow in a Newtonian curved squeeze film using EIM, by Han and Rogers³⁵ on modeling squeeze film force for large amplitude motion in a two dimensional squeeze film using an elliptical velocity profile and by Usha and Vimala³⁶ on squeeze film force modeling in a circular squeeze film using EIM have been shown to be in good agreement either with experimental results or with the numerical solutions^{37–40} and have thus justified the validity of applying EIM in lubrication problems, in particular, in squeeze flow problems. It is worth mentioning here that EIM applied to squeeze flow problems not only predicts the squeeze film force at small to moderate Reynolds numbers accurately, but also predicts it for large amplitude motion. The success of the EIM in effectively and accurately predicting the squeeze film force in squeeze flow problems and in predicting the inertial effects on the performance of

squeeze film dampers has given the confidence to use this simple, yet more accurate method in the investigation of the evolution of waves on a viscous Newtonian film flowing down an inclined plane or vertical wall.

In view of this, a model describing the evolution of waves on a Newtonian fluid film down an inclined plane using EIM with self-similar velocity profile assumption has been presented for high Reynolds numbers and moderate Weber numbers. It is worth mentioning here that the investigation presents another way of simplifying the Navier–Stokes equations for the falling film problem; instead of the classical approach of averaging the tangential momentum across the film to obtain an integral equation of motion [momentum integral method (MIM)], the present formulation uses a velocity weighted average, namely the depth averaged kinetic energy balance (energy integral method).

The objective of this averaging is to remove the dependence in the normal direction and hence reduce the spatial dimension by one. The main key of this approach is to retain the dynamic inertial term in the momentum equation. The present approach is a reasonable alternative to the more classical approach using MIM. The averaging methods which are *ad hoc* approximations intended for high Reynolds numbers are similar to using different bases functions or different weighting functions in a truncated Galerkin expansion in numerical spectral methods. Therefore, these methods can be considered as a particular truncation of the exact Petrov–Galerkin method. The simplest of such averaging methods yields the Shkadov model,¹² which assumes a lubrication like parabolic velocity. Nguyen and Balakotiah,⁴¹ Ooshida⁴² and Ruyer-Quil and Manneville⁴³ have used different bases. Ruyer-Quil and Manneville⁴³ have developed a model equation describing the evolution of a thin film down an incline using Gradient expansion method. Nguyen and Balakotiah⁴¹ and Yu *et al.*⁴⁹ have used different velocity profiles in the modeling of evolution equation. Ooshida⁴² has produced an estimate of the error and has accelerated the convergence with a Padé approximation.

Chang and Demekhin,⁴⁴ in an attempt to implement the idea that in the long wave expansion the flow variables are strictly enslaved by the local thickness of the film, have presented the governing evolution equation for the local thickness using the Petrov–Galerkin method. Following the approach suggested by Ruyer-Quil and Manneville⁴³ and Nguyen and Balakotiah⁴¹ and choosing a specific extension of the one-mode approximation in the Petrov–Galerkin method, Chang and Demekhin⁴⁴ have obtained a hierarchy of model equations. Thus, in the study of dynamics and stability characteristics of waves on thin inclined/vertical Newtonian films, a series of simplified equations have been developed over the last three decades for modeling film flows, starting from the full Navier–Stokes equations and using various approximations and different methods for various order of magnitude assumptions of the pertinent dimensionless Reynolds number and Weber number. The accuracy of these models has been tested either by comparing the amplitude and shape of a fully developed wave^{41,43} with that observed in the experiment or the wave speed and amplitude of the

primary solitary wave⁴⁴ with that predicted by the numerical solution of Navier–Stokes equations.

In the present study, the film flow down an inclined plane is modeled by two nonlinear partial differential equations which describe the temporal and spatial evolution of local volumetric discharge rate and local flow layer depth and they are obtained by including consistently all the terms up to $O(\epsilon^2)$ in the Navier–Stokes equations, for $Re \approx O(\epsilon^{-1})$ and $We \approx O(1)$. As the results of the linear stability theory can detect any inadequacies in the simplified models near wave inception, it is used as a primary criterion for model discrimination and the neutral stability curves generated from the two models based on MIM⁴⁵ and EIM (present study) are compared with the experimental results for vertically falling films. It is observed that the linearized theory of the present study is supported by experimental evidence in the parametric regime of interest. The results show that the present model can describe the dynamics of wave evolution on a falling liquid film for Re up to 100.

It is of interest to see how well the present model captures the physical phenomena exhibited by the earlier models and the experiments, and in view of this, attention is focused on the stationary waves of finite-amplitude and long wavelength on a thin viscous film down an inclined plane at high Reynolds numbers and moderate Weber numbers.

The study is similar to the theoretical investigation on the finite-amplitude waves of stationary form on a thin film of viscous fluid flowing down an inclined plane at high Reynolds numbers and moderate Weber numbers using the MIM by Lee and Mei.⁴⁵ In the frame of reference moving with the steady wave speed, the approximate equations accurate to the second order in the depth to wavelength ratio are reduced to a third order dynamical system. The experiments by Liu and Gollub⁵² demonstrate that, farther downstream, the film flows produced by either regular high frequency forcing or by natural noise are eventually dominated by a small number of irregularly spaced solitary humps, which emerge through phenomena of period-doubling and wave merging. Motivated by the experimental results by Chu and Duckler^{46,47} and Takahama and Kato,⁴⁸ which indicate the predominance of irregular chaotic waves sufficiently downstream, the present study considers the possible bifurcations of film waves that may happen far downstream. Using modern bifurcation techniques of dynamical systems theory, it is shown that in the regime where sinusoidal waves are linearly unstable, uniform flows corresponding to the fixed points of the reduced system undergo Hopf bifurcation. Complex bifurcation scenarios after the onset of limit cycles are presented using the numerical integration of the dynamical system. The highest period-1 waves taken at the threshold where the first fixed point H_1 bifurcates to a period-2 limit cycle has been adopted as the theoretical periodic wave for each fixed Re . The theoretical predictions of Hopf thresholds and the limiting speeds are presented.

Thus, our objectives in this investigation are as follows.

- (i) To present a new model (EIM) by using a different averaging procedure in the derivation of the evolution equation.

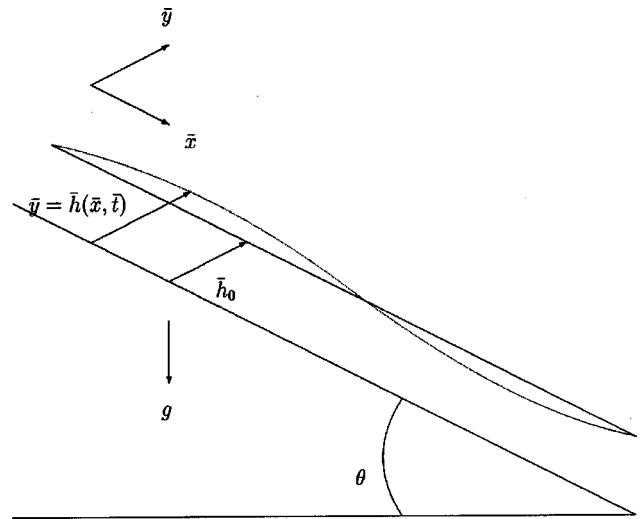


FIG. 1. Schematic representation of a thin film flow down an inclined plane.

- (ii) To see how well the present model (EIM) exhibits the different dynamical phenomena demonstrated by the earlier model (MIM) and the experiments.^{46–48,52}
- (iii) To look for similarities and differences between the two models (EIM and MIM).

The development of different models either by adopting different methods or by using different profiles to approximate the unknown functions are needed and it is for this reason that the present investigation has been considered with the above objectives.

II. MATHEMATICAL FORMULATION

The two dimensional flow of a thin layer of an incompressible Newtonian fluid down an inclined plane is considered. The flow depth is denoted by $\bar{h}(\bar{x}, \bar{t})$ and the angle of inclination of the plane bottom with respect to the horizontal is denoted by θ , where $0 < \theta \leq \pi/2$. A rectangular coordinate system is chosen with an \bar{x} -axis coinciding with the plane bottom and the \bar{y} -axis pointing vertically upwards from the inclined plane (Fig. 1). The governing equations are

$$\frac{\partial \bar{u}}{\partial \bar{x}} + \frac{\partial \bar{v}}{\partial \bar{y}} = 0, \quad (1)$$

$$\rho \left(\frac{\partial \bar{u}}{\partial \bar{t}} + \bar{u} \frac{\partial \bar{u}}{\partial \bar{x}} + \bar{v} \frac{\partial \bar{u}}{\partial \bar{y}} \right) = - \frac{\partial \bar{p}}{\partial \bar{x}} + \rho g \sin \theta + \mu \left(\frac{\partial^2 \bar{u}}{\partial \bar{x}^2} + \frac{\partial^2 \bar{u}}{\partial \bar{y}^2} \right), \quad (2)$$

$$\rho \left(\frac{\partial \bar{v}}{\partial \bar{t}} + \bar{u} \frac{\partial \bar{v}}{\partial \bar{x}} + \bar{v} \frac{\partial \bar{v}}{\partial \bar{y}} \right) = - \frac{\partial \bar{p}}{\partial \bar{y}} - \rho g \cos \theta + \mu \left(\frac{\partial^2 \bar{v}}{\partial \bar{x}^2} + \frac{\partial^2 \bar{v}}{\partial \bar{y}^2} \right), \quad (3)$$

where \bar{u} , \bar{v} denote the velocity components in the \bar{x} and \bar{y} increasing directions, \bar{p} the pressure, ρ the density, g the gravitational acceleration and μ the coefficient of viscosity of the fluid. The boundary conditions are

$$\bar{u} = 0, \bar{v} = 0, \text{ on } \bar{y} = 0 \quad (\text{no-slip condition}); \tag{4}$$

$$\begin{aligned} \bar{p} - \bar{p}_a - 2 \left\{ \mu \left[\frac{\partial \bar{u}}{\partial \bar{x}} \left(\frac{\partial \bar{h}}{\partial \bar{x}} \right)^2 - \left(\frac{\partial \bar{u}}{\partial \bar{y}} + \frac{\partial \bar{v}}{\partial \bar{x}} \right) \frac{\partial \bar{h}}{\partial \bar{x}} + \frac{\partial \bar{v}}{\partial \bar{y}} \right] \right. \\ \left. \times \left[1 + \left(\frac{\partial \bar{h}}{\partial \bar{x}} \right)^2 \right]^{-1} + \sigma \frac{\partial^2 \bar{h}}{\partial \bar{x}^2} \left[1 + \left(\frac{\partial \bar{h}}{\partial \bar{x}} \right)^2 \right]^{-3/2} \right\} = 0, \end{aligned} \tag{5}$$

on $\bar{y} = \bar{h}$ (continuity of the normal stress at the free surface);

$$\left\{ -4 \frac{\partial \bar{u}}{\partial \bar{x}} \frac{\partial \bar{h}}{\partial \bar{x}} + \left(\frac{\partial \bar{u}}{\partial \bar{y}} + \frac{\partial \bar{v}}{\partial \bar{x}} \right) \left(1 - \left(\frac{\partial \bar{h}}{\partial \bar{x}} \right)^2 \right) \right\} = 0, \tag{6}$$

on $\bar{y} = \bar{h}$ (continuity of the shear stress at the free surface);

$$\frac{\partial \bar{h}}{\partial \bar{t}} + \bar{u} \frac{\partial \bar{h}}{\partial \bar{x}} - \bar{v} = 0, \tag{7}$$

on $\bar{y} = \bar{h}$ (kinematic boundary condition);

where σ is the interfacial surface tension coefficient.

The dimensionless form of the above governing equations is obtained by choosing scales based on the primary flow given by

$$\bar{u} = \frac{g \sin \theta \bar{h}_0^2}{2\nu} \left[\frac{2\bar{y}}{\bar{h}_0} - \frac{\bar{y}^2}{\bar{h}_0^2} \right], \bar{v} = 0, \tag{8}$$

where \bar{h}_0 is the unperturbed uniform flow depth. The primary flow corresponds to the solution for uniform flow and the depth averaged velocity is

$$\bar{u}_0 = \frac{1}{\bar{h}_0} \int_0^{\bar{h}_0} \bar{u} \, d\bar{y} = \frac{g \sin \theta \bar{h}_0^2}{3\nu}, \tag{9}$$

and the corresponding volume-discharge rate is

$$\bar{q}_0 = \bar{u}_0 \bar{h}_0. \tag{10}$$

The dimensionless quantities are defined as

$$\begin{aligned} x = \frac{\bar{x}}{L}, \quad y = \frac{\bar{y}}{\bar{h}_0}, \quad H = \frac{\bar{h}}{\bar{h}_0}, \quad u = \frac{\bar{u}}{\bar{u}_0}, \quad v = \frac{L\bar{v}}{\bar{h}_0\bar{u}_0}, \\ t = \frac{\bar{u}_0 \bar{t}}{L}, \quad p = \frac{\bar{p} - \bar{p}_a}{\rho \bar{u}_0^2}, \quad \epsilon = \frac{\bar{h}_0}{L}, \end{aligned} \tag{11}$$

where the longitudinal length scale L is associated with the characteristic wavelength on the free surface and is of the same order as that of the wavelength. It is assumed that the layer is shallow so that the depth to wavelength ratio is small. Using (11) in (1)–(7), the nondimensional equations and boundary conditions are obtained as

$$\frac{\partial u}{\partial x} + \frac{\partial v}{\partial y} = 0, \tag{12}$$

$$\begin{aligned} \left(\frac{\partial u}{\partial t} + u \frac{\partial u}{\partial x} + v \frac{\partial u}{\partial y} \right) \\ = - \frac{\partial p}{\partial x} + \frac{3}{\epsilon \text{Re}} + \frac{\epsilon}{\text{Re}} \frac{\partial^2 u}{\partial x^2} + \frac{1}{\epsilon \text{Re}} \frac{\partial^2 u}{\partial y^2}, \end{aligned} \tag{13}$$

$$\begin{aligned} \epsilon^2 \left(\frac{\partial v}{\partial t} + u \frac{\partial v}{\partial x} + v \frac{\partial v}{\partial y} \right) \\ = - \frac{\partial p}{\partial y} - \frac{3 \cot \theta}{\text{Re}} + \frac{\epsilon^3}{\text{Re}} \frac{\partial^2 v}{\partial x^2} + \frac{\epsilon}{\text{Re}} \frac{\partial^2 v}{\partial y^2}, \end{aligned} \tag{14}$$

$$u = 0, v = 0, \text{ on } y = 0; \tag{15}$$

$$\begin{aligned} p + \frac{2\epsilon}{\text{Re}} \left(\frac{\partial u}{\partial y} \frac{\partial H}{\partial x} + \epsilon^2 \frac{\partial v}{\partial x} \frac{\partial H}{\partial x} - \epsilon^2 \frac{\partial u}{\partial x} \left(\frac{\partial H}{\partial x} \right)^2 - \frac{\partial v}{\partial y} \right) \\ \times \left[1 + \epsilon^2 \left(\frac{\partial H}{\partial x} \right)^2 \right]^{-1} + \epsilon^2 \text{We} \frac{\partial^2 H}{\partial x^2} \left[1 + \epsilon^2 \left(\frac{\partial H}{\partial x} \right)^2 \right]^{-3/2} \\ = 0, \text{ on } y = H; \end{aligned} \tag{16}$$

$$\begin{aligned} \left(\frac{\partial u}{\partial y} + \epsilon^2 \frac{\partial v}{\partial x} \right) \left[1 - \epsilon^2 \left(\frac{\partial H}{\partial x} \right)^2 \right] + 2\epsilon^2 \left(\frac{\partial v}{\partial y} - \frac{\partial u}{\partial x} \right) \frac{\partial H}{\partial x} = 0, \\ \text{on } y = H; \end{aligned} \tag{17}$$

$$v = \frac{\partial H}{\partial t} + u \frac{\partial H}{\partial x}, \text{ at } y = H; \tag{18}$$

where $\text{Re} = \bar{u}_0 \bar{h}_0 / \nu = g \sin \theta \bar{h}_0^3 / 3\nu^2$ is the Reynolds number; $\text{We} = \sigma / \rho \bar{u}_0^2 \bar{h}_0$ is the Weber number.

In what follows, a model based on self-similar parabolic velocity profile assumption (two equation model) has been obtained by using energy integral method and the linear instability of the uniform flow has been discussed.

III. TWO EQUATION MODEL

The two equation model describing the temporal and spatial evolution of the local flow rate $Q(x, t)$ and the local flow depth $H(x, t)$ is obtained from Eqs. (12)–(18) using EIM with a self-similar velocity profile assumption by including terms up to $O(\epsilon^2)$, when $\text{Re} \approx O(\epsilon^{-1})$ and $\text{We} \approx O(1)$.

The exact solution for the uniform primary flow described by the parabolic velocity profile,

$$u = \frac{3Q}{2H} \left(\frac{2y}{H} - \frac{y^2}{H^2} \right), \tag{19}$$

is assumed, where

$$Q = \int_0^H u \, dy.$$

The velocity component in the y -direction is obtained from Eqs. (12) and (15) as

$$v = -y^2 \left(\frac{3Q_x}{2H^2} - \frac{3QH_x}{H^3} \right) + y^3 \left(\frac{Q_x}{2H^3} - \frac{3QH_x}{2H^4} \right). \quad (20) \quad \frac{\partial u}{\partial y} = \epsilon^2 \left(4 \frac{\partial u}{\partial x} \frac{\partial H}{\partial x} - \frac{\partial v}{\partial x} \right), \quad \text{on } y=H. \quad (22)$$

Equations (16) and (17) are simplified to

$$p = \frac{2\epsilon}{\text{Re}} \frac{\partial v}{\partial y} - \epsilon^2 \text{We} \frac{\partial^2 H}{\partial x^2}, \quad \text{on } y=H; \quad (21) \quad \text{Using Eqs. (19) and (20), the pressure distribution is obtained from Eq. (14) as}$$

$$p = \frac{\epsilon}{\text{Re}} \left[\left(-\frac{3Q_x}{2H} + \frac{3QH_x}{2H^2} \right) + \left(-\frac{3Q_x}{H^2} + \frac{6QH_x}{H^3} \right) y + \left(\frac{3Q_x}{2H^3} - \frac{9QH_x}{2H^4} \right) y^2 \right] + \epsilon^2 \left[-\text{We} H_{xx} + \left(-\frac{3HQ_{xt}}{8} + \frac{5H_t Q_x}{8} + \frac{5H_x Q_t}{8} \right. \right. \\ \left. \left. + \frac{5H_{xt} Q}{8} - \frac{3H_x H_t Q}{2H} - \frac{QQ_{xx}}{2} - \frac{33H_x^2 Q^2}{40H^2} + \frac{33H_{xx} Q^2}{40H} + \frac{Q_x^2}{2} + \frac{3H_x QQ_x}{20H} \right) + \left(\frac{Q_{xt}}{2H^2} - \frac{H_t Q_x}{H^3} - \frac{H_x Q_t}{H^3} - \frac{H_{xt} Q}{H^3} \right. \right. \\ \left. \left. + \frac{3H_x H_t Q}{H^4} \right) y^3 + \left(-\frac{Q_{xt}}{8H^3} + \frac{3H_t Q_x}{8H^4} + \frac{3H_x Q_t}{8H^4} + \frac{3H_{xt} Q}{8H^4} - \frac{3H_x H_t Q}{2H^5} + \frac{9QQ_{xx}}{8H^4} - \frac{9H_{xx} Q^2}{4H^5} + \frac{9H_x^2 Q^2}{4H^6} - \frac{9Q_x^2}{8H^4} \right) y^4 \\ \left. + \left(-\frac{3QQ_{xx}}{4H^5} - \frac{3H_x QQ_x}{20H^6} + \frac{9H_{xx} Q^2}{5H^6} - \frac{9H_x^2 Q^2}{5H^7} + \frac{3Q_x^2}{4H^5} \right) y^5 + \left(\frac{QQ_{xx}}{8H^6} - \frac{3H_{xx} Q^2}{8H^7} + \frac{3H_x^2 Q^2}{8H^8} - \frac{Q_x^2}{8H^6} \right) y^6 \right] + \frac{3 \cot \theta}{\text{Re}} (H-y). \quad (23)$$

If the bottom is nearly horizontal, say $\cot \theta \approx O(\epsilon^{-1})$, then the last term in Eq. (23) is of order one and the leading order pressure distribution is of order unity and nearly hydrostatic. If the flow is down a vertical plate, $\cot \theta = 0$, the pressure distribution is of $O(\epsilon^2)$. For any finite bottom slope of the inclined plane with $\tan \theta \approx O(1)$, the pressure is of $O(\epsilon)$. Integration of the continuity equation (12) with respect to y from $y=0$ to $y=H$ along with the boundary condition (18) yields

$$H_t + Q_x = 0. \quad (24)$$

Multiplying the x -momentum equation (13) with u and integrating the resulting equation with respect to y from $y=0$ to $y=H$, gives

$$\int_0^H \left\{ u \left(\frac{\partial u}{\partial t} + u \frac{\partial u}{\partial x} + v \frac{\partial u}{\partial y} \right) + u \frac{\partial p}{\partial x} - \frac{3}{\epsilon \text{Re}} u - \frac{\epsilon}{\text{Re}} u \frac{\partial^2 u}{\partial x^2} - \frac{1}{\epsilon \text{Re}} u \frac{\partial^2 u}{\partial y^2} \right\} dy = \sum_{i=1}^5 t_i = 0, \quad (25)$$

where

$$t_1 = \int_0^H u \left(\frac{\partial u}{\partial t} + u \frac{\partial u}{\partial x} + v \frac{\partial u}{\partial y} \right) dy = \int_0^H \left\{ \frac{\partial}{\partial t} \left(\frac{u^2}{2} \right) + \frac{\partial}{\partial x} \left(\frac{u^3}{2} \right) + \frac{\partial}{\partial y} \left(\frac{u^2 v}{2} \right) \right\} dy = \frac{6QQ_t}{5H} - \frac{3H_t Q^2}{5H^2} + \frac{81Q^2 Q_x}{35H^2} - \frac{54H_x Q^3}{35H^3}, \quad (26)$$

$$t_2 = \int_0^H u \frac{\partial p}{\partial x} dy = \frac{3 \cot \theta}{\text{Re}} QH_x - \epsilon^2 \text{We} QH_{xxx} - \frac{\epsilon}{\text{Re}} \left[\frac{27QQ_{xx}}{10H} - \frac{129QQ_x H_x}{20H^2} - \frac{129Q^2 H_{xx}}{40H^2} + \frac{123Q^2 H_x^2}{20H^3} \right] \\ + \epsilon^2 Q \left[-\frac{33H_x Q_{xt}}{140} - \frac{33HQ_{xxt}}{140} + \frac{107H_t Q_{xx}}{280} + \frac{107H_{xt} Q_x}{140} + \frac{107H_{xx} Q_t}{280} + \frac{107H_{xxt} Q}{280} - \frac{9H_x H_t Q_x}{35H} \right. \\ \left. - \frac{123H_t H_{xx} Q}{140H} + \frac{87H_x^2 Q_t}{140H} - \frac{9H_x H_{xt} Q}{35H} - \frac{39H_t H_x^2 Q}{70H^2} + \frac{Q_x Q_{xx}}{3} - \frac{QQ_{xxx}}{3} + \frac{533H_{xx} QQ_x}{448H} + \frac{241H_{xxx} Q^2}{448H} \right. \\ \left. - \frac{333H_x H_{xx} Q^2}{448H^2} - \frac{113H_x^2 QQ_x}{112H^2} + \frac{23H_x^3 Q^2}{112H^3} + \frac{73H_x Q_x^2}{112H} - \frac{95H_x QQ_{xx}}{224H} \right], \quad (27)$$

$$t_3 = -\frac{3}{\epsilon \text{Re}} \int_0^H u dy = -\frac{3Q}{\epsilon \text{Re}}, \quad (28)$$

$$t_4 = -\frac{\epsilon}{\text{Re}} \int_0^H u \frac{\partial^2 u}{\partial x^2} dy = -\frac{\epsilon}{\text{Re}} \left[\frac{6QQ_{xx}}{5H} - \frac{69QQ_x H_x}{20H^2} - \frac{69Q^2 H_{xx}}{40H^2} + \frac{63Q^2 H_x^2}{20H^3} \right], \quad (29)$$

$$t_5 = -\frac{1}{\epsilon \text{Re}} \int_0^H u \frac{\partial^2 u}{\partial y^2} dy = -\frac{\epsilon}{\text{Re}} \left[\frac{3QQ_{xx}}{2H} + \frac{9QQ_x H_x}{2H^2} - \frac{9Q^2 H_{xx}}{4H^2} - \frac{9Q^2 H_x^2}{2H^3} \right] + \frac{1}{\epsilon \text{Re}} \frac{3Q^2}{H^3}. \quad (30)$$

In the derivation of (26)–(30), Eqs. (15), (19), (20), and (22) have been used. Substituting for $t_i, i=1,2,\dots,5$ in (25), the governing equation is obtained as

$$\left\{ \frac{6Q_t}{5H} - \frac{3H_t Q}{5H^2} + \frac{81QQ_x}{35H^2} - \frac{54H_x Q^2}{35H^3} - \frac{3}{\epsilon \text{Re}} + \frac{1}{\epsilon \text{Re}} \frac{3Q}{H^3} + \frac{3 \cot \theta}{\text{Re}} H_x + \epsilon^2 \left[-\text{We} H_{xxx} - \frac{33H_x Q_{xt}}{140} - \frac{33H Q_{xxt}}{140} + \frac{107H_t Q_{xx}}{280} \right. \right. \\ \left. \left. + \frac{107H_{xt} Q_x}{140} + \frac{107H_{xx} Q_t}{280} + \frac{107H_{xxt} Q}{280} - \frac{9H_x H_t Q_x}{35H} - \frac{123H_t H_{xx} Q}{140H} + \frac{87H_x^2 Q_t}{140H} - \frac{9H_x H_{xt} Q}{35H} - \frac{39H_t H_x^2 Q}{70H^2} + \frac{Q_x Q_{xx}}{3} \right. \\ \left. - \frac{QQ_{xxx}}{3} + \frac{533H_{xx} QQ_x}{448H} + \frac{241H_{xxx} Q^2}{448H} - \frac{333H_x H_{xx} Q^2}{448H^2} - \frac{113H_x^2 QQ_x}{112H^2} + \frac{23H_x^3 Q^2}{112H^3} + \frac{73H_x Q_x^2}{112H} - \frac{95H_x QQ_{xx}}{224H} \right] \\ \left. - \frac{\epsilon}{\text{Re}} \left[\frac{27Q_{xx}}{5H} - \frac{27H_x Q_x}{5H^2} - \frac{36H_{xx} Q}{5H^2} + \frac{24H_x^2 Q}{5H^3} \right] \right\} = 0. \tag{31}$$

Equations (24) and (31) describe the spatial and temporal evolution of $Q(x,t)$ and $H(x,t)$.

A. Linear instability of the uniform flow

If η and q denote the infinitesimal disturbances from the uniform flow, $H=1+\eta$, $Q=1+q$, then the linearization of Eqs. (24) and (31) and the elimination of q gives

$$\frac{6}{5} \eta_{tt} + \frac{102}{35} \eta_{xt} + \frac{54}{35} \eta_{xx} + \frac{3}{\epsilon \text{Re}} (\eta_t + 3 \eta_x) - \frac{3 \cot \theta}{\text{Re}} \eta_{xx} \\ - \frac{\epsilon}{\text{Re}} \left[\frac{27}{5} \eta_{xxt} + \frac{36}{5} \eta_{xxx} \right] - \epsilon^2 \left[-\text{We} \eta_{xxx} + \frac{33}{140} \eta_{xxtt} \right. \\ \left. + \frac{601}{840} \eta_{xxxt} + \frac{241}{448} \eta_{xxxx} \right] = 0. \tag{32}$$

By considering a wave like disturbance,

$$\eta = e^{i(x-ct)}, \tag{33}$$

and substituting (33) in (32), a characteristic equation for the complex phase velocity $c=c_r+ic_i$ is obtained as

$$\left(1 + \frac{11}{56} \epsilon^2 \right) c^2 + \left(i \left[\frac{5}{2\epsilon \text{Re}} + \frac{9\epsilon}{2\text{Re}} \right] - \frac{17}{7} - \frac{601}{1008} \epsilon^2 \right) c \\ + \left(-i \left[\frac{15}{2\epsilon \text{Re}} + \frac{6\epsilon}{\text{Re}} \right] + \frac{9}{7} - \frac{5 \cot \theta}{2\text{Re}} - \frac{5}{6} \epsilon^2 \text{We} \right. \\ \left. + \frac{1205}{2688} \epsilon^2 \right) = 0. \tag{34}$$

It is to be noted that the normalizing length (L) is chosen to be the reciprocal of the wave number ($1/a$) in physical dimensions so that ϵ in (32) is $a\bar{h}_0$. The stability of the primary flow is determined by the sign of c_i . If $c_i > 0$, the

primary flow is unstable, whereas if $c_i < 0$, the primary flow is stable. The solution of (34) which corresponds to a stable mode is given by

$$c_r = \frac{\left(\left(\frac{17}{7} + \frac{601}{1008} \epsilon^2 \right) - \sqrt{\frac{\sqrt{A^2+B^2}+A}{2}} \right)}{2 \left(1 + \frac{11}{56} \epsilon^2 \right)}, \\ c_i = \frac{\left(- \left(\frac{5}{2\epsilon \text{Re}} + \frac{9\epsilon}{2\text{Re}} \right) - \sqrt{\frac{\sqrt{A^2+B^2}-A}{2}} \right)}{2 \left(1 + \frac{11}{56} \epsilon^2 \right)}, \tag{35}$$

where

$$A = \left(\frac{17}{7} + \frac{601}{1008} \epsilon^2 \right)^2 - \left(\frac{5}{2\epsilon \text{Re}} + \frac{9\epsilon}{2\text{Re}} \right)^2 - 4 \left(1 + \frac{11}{56} \epsilon^2 \right) \\ \times \left(\frac{9}{7} - \frac{5 \cot \theta}{2\text{Re}} - \frac{5}{6} \epsilon^2 \text{We} + \frac{1205}{2688} \epsilon^2 \right), \\ B = 4 \left(1 + \frac{11}{56} \epsilon^2 \right) \left(\frac{15}{2\epsilon \text{Re}} \right) + \frac{6\epsilon}{\text{Re}} - 2 \left(\frac{17}{7} + \frac{601}{1008} \epsilon^2 \right) \\ \times \left(\frac{5}{2\epsilon \text{Re}} + \frac{9\epsilon}{2\text{Re}} \right). \tag{36}$$

The phase velocity and growth rate of the potentially unstable mode is given by

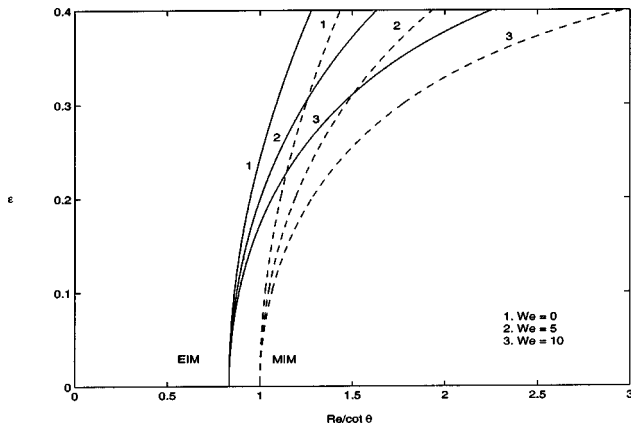


FIG. 2. Neutral curves in the ϵ versus $Re/\cot \theta$ plane for various Weber numbers.

$$c_r = \frac{\left(\left(\frac{17}{7} + \frac{601}{1008} \epsilon^2 \right) + \sqrt{\frac{\sqrt{A^2 + B^2} + A}{2}} \right)}{2 \left(1 + \frac{11}{56} \epsilon^2 \right)},$$

$$c_i = \frac{\left(- \left(\frac{5}{2\epsilon Re} + \frac{9\epsilon}{2 Re} \right) + \sqrt{\frac{\sqrt{A^2 + B^2} - A}{2}} \right)}{2 \left(1 + \frac{11}{56} \epsilon^2 \right)}. \quad (37)$$

The threshold for linear stability or neutral stability is obtained from (37) by setting $c_i = 0$. It is observed that on the plane of $Re/\cot \theta$ versus ϵ , there are three branches of neutral curves, for a given Weber number We . They are the $Re/\cot \theta$ -axis, the ϵ -axis and the curve given by

$$\frac{Re}{\cot \theta} = \frac{\left(\frac{5}{6} + 3\epsilon^2 \right)}{1 - \frac{5}{18} We \epsilon^2 + \frac{16093}{94080} \epsilon^2}$$

$$= \frac{5}{6} + \epsilon^2 \left[3 - \frac{5}{6} \left(\frac{5}{18} We - \frac{16093}{94080} \right) \right] + O(\epsilon^4). \quad (38)$$

The neutral curves for various Weber numbers using MIM⁴⁵ and EIM are plotted in Fig. 2. The primary flow is unstable in the region bounded by the $Re/\cot \theta$ axis and the neutral curve plotted in Fig. 2. There is a reduction in the region of instability as the Weber number increases, showing that the effect of surface tension is to stabilize the primary flow. The disturbances of the infinitely long waves are obtained from (38) by taking $\epsilon = 0$ and this yields the critical condition for instability as

$$\frac{\cot \theta}{Re} = \frac{6}{5}. \quad (39)$$

Therefore, the region of linear instability is $0 \leq \cot \theta/Re < 6/5$ while $\cot \theta/Re > 6/5$ is the region of linear stability.

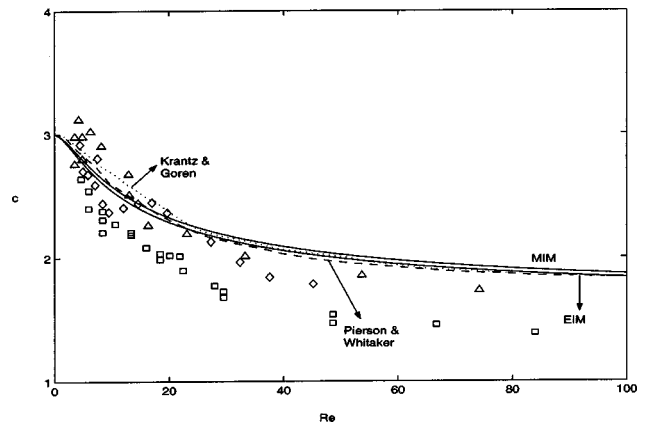


FIG. 3. Dimensionless wave speed for vertically falling water films. \square : expt. by Jones and Whitaker (Ref. 53); \diamond : expt. by Stainthorp and Allen (Ref. 54); \triangle : expt. by Strobel and Whitaker (Ref. 55).

It is worth mentioning here that the linear instability threshold predicted by the present model (EIM) agrees with the classical result of the Orr–Sommerfeld analysis for a small Reynolds number flow^{50,51} and verified experimentally by Liu and Gollub.⁵² On the other hand, the momentum integral method (MIM) predicts the range of linear instability as $0 \leq \cot \theta/Re < 1$. Figure 3 shows the linear predictions of the phase velocity of the fastest growing wave by the present model, the model by Lee and Mei⁴⁵ (which uses MIM¹⁶), the experimental^{53–55} results observed near the inception region for vertically falling film flows of water for $Re \leq 100$, approximate solutions from the momentum integral form of the Orr–Sommerfeld equation by Krantz and Goren⁵⁶ and the direct numerical solutions of the Orr–Sommerfeld equation by Pierson and Whitaker.⁵⁷ The results show that both the energy integral and momentum integral models agree well with the experimental predictions thus supporting the validity of the linearised theory in the parametric regime $Re \approx O(\epsilon^{-1})$.

IV. THE GOVERNING EQUATIONS FOR STATIONARY WAVES

A second order theory for permanent waves which propagate at a constant speed without any change in form is

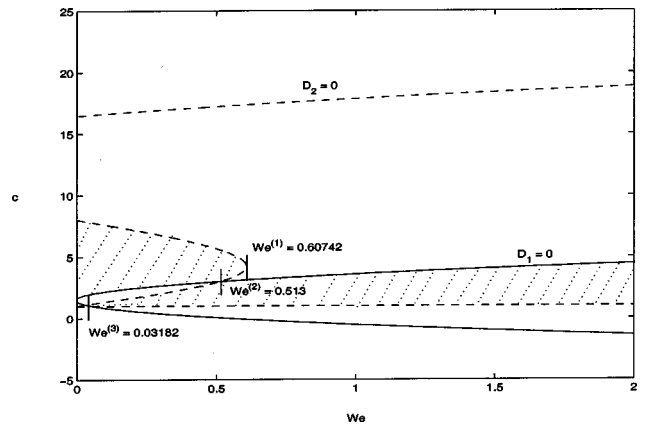


FIG. 4. Parameter regimes delimited for $H_I = H_s$ and $H_{II} = H_s$. Heteroclinic orbits exist only in the shaded regions.

pursued in this section. While wave transitions in real-life involve complex spatio-temporal dynamics and many of these transitions lead to chaotic waves that are not stationary traveling waves, in what follows, the bifurcation of stationary traveling waves has been examined as a preliminary study of the more complex transitions. The governing equations are obtained from (24) and (31) by transforming to a moving coordinate system defined by $\xi = (1/\epsilon)(x - ct)$, where c is the propagation speed. Using the relations

$$\frac{\partial}{\partial x} = \frac{\partial}{\partial \xi}, \quad \frac{\partial}{\partial t} = -c \frac{\partial}{\partial \xi} \tag{40}$$

and

$$Q = c(H - 1) + 1, \tag{41}$$

obtained from (24), the third order ordinary differential equation for the flow depth is obtained as

$$\begin{aligned} & \left\{ H_{\xi\xi\xi} \left[\frac{391}{6720} c^2 H^4 + \frac{1211}{3360} c H^3 (1 - c) + \frac{241}{448} H^2 (1 - c)^2 - \text{We} H^3 \right] + \frac{H_{\xi\xi}}{\text{Re}} \left[\frac{9}{5} c H^2 + \frac{36}{5} H (1 - c) \right] \right. \\ & + H_{\xi} \left[\frac{6}{35} c^2 H^2 - \frac{6}{35} c H (1 - c) - \frac{54}{35} (1 - c)^2 + \frac{3 \cot \theta}{\text{Re}} H^3 \right] + H_{\xi} H_{\xi\xi} \left[- \frac{379}{1680} c^2 H^3 - \frac{21}{2240} c H^2 (1 - c) - \frac{333}{448} H (1 - c)^2 \right] \\ & \left. + \frac{H_{\xi}^2}{\text{Re}} \left[\frac{3}{5} c H - \frac{24}{5} (1 - c) \right] + H_{\xi}^2 \left[\frac{23}{560} c^2 H^2 + \frac{27}{560} c H (1 - c) + \frac{23}{112} (1 - c)^2 \right] - \frac{3}{\text{Re}} (H - 1)(H^2 + H + 1 - c) \right\} = 0. \end{aligned} \tag{42}$$

By this coordinate renormalization, the new horizontal length scale is the primary flow depth \bar{h}_0 and the highest derivative appears at the leading order in ϵ . It is assumed that the primary flow given by $H^* = 1, Q^* = 1$ is approached either far upstream $\xi = -\infty$ or far downstream $\xi = +\infty$. The flow is governed by four physical parameters $\text{Re}, \text{We}, \theta$ and c . Equation (42) is expressed as a three dimensional dynamical system by the differential equations

$$\begin{aligned} H_{\xi} &= \bar{H}, \\ \bar{H}_{\xi} &= \bar{\bar{H}}, \\ \bar{\bar{H}}_{\xi} &= \frac{F(H, \bar{H}, \bar{\bar{H}}; \cot \theta / \text{Re}, \text{Re}, c)}{D(H; \text{We}, c)}, \end{aligned} \tag{43}$$

where H represents the flow depth, $\bar{H} = H_{\xi}$ represents the slope, $\bar{\bar{H}} = H_{\xi\xi}$ represents the curvature of the free surface and

$$\begin{aligned} D &= \text{We} H - \frac{391}{6720} c^2 H^2 + \frac{1211}{3360} c H (c - 1) - \frac{241}{448} (1 - c)^2, \\ F &= \left\{ \bar{H} \left[\frac{6}{35} c^2 H^2 - \frac{6}{35} c H (1 - c) - \frac{54}{35} (1 - c)^2 + \frac{3 \cot \theta}{\text{Re}} H^3 \right] + \frac{\bar{\bar{H}}}{\text{Re}} \left[\frac{9}{5} c H^2 + \frac{36}{5} H (1 - c) \right] + \bar{H} \bar{\bar{H}} \left[- \frac{379}{1680} c^2 H^3 \right. \right. \\ & - \frac{21}{2240} c H^2 (1 - c) - \frac{333}{448} H (1 - c)^2 \left. \right] + \frac{\bar{H}^2}{\text{Re}} \left[\frac{3}{5} c H - \frac{24}{5} (1 - c) \right] + \bar{H}^3 \left[\frac{23}{560} c^2 H^2 + \frac{27}{560} c H (1 - c) + \frac{23}{112} (1 - c)^2 \right] \\ & \left. - \frac{3}{\text{Re}} (H - 1)(H^2 + H + 1 - c) \right\}. \end{aligned} \tag{45}$$

The fixed points are obtained by equating the right hand side of Eq. (43) to zero and are given by $H_I = (H, \bar{H}, \bar{\bar{H}}) = (1, 0, 0)$ and $H_{II} = ((-1 + \sqrt{4c - 3})/2, 0, 0)$. The fixed point H_I corresponds to the uniform primary flow. The fixed point H_{II} , is a function of c and is real and positive only for $c > 1$. Therefore, this corresponds to an asymptotic part of a nonuniform profile propagating at a speed $c > 1$. The fixed points are independent of θ, Re and We and at $c = 3, H_I$ and H_{II} cross each other, implying that a transcritical bifurcation exists at $c = 3$ at which the two fixed points exchange their

stability properties. The parameter c is taken as the bifurcation parameter for chosen values of other physical parameters.

A. Search for heteroclinic orbits

It is of interest to look for heteroclinic orbits connecting the two fixed points in the three dimensional phase space $(H, \bar{H}, \bar{\bar{H}})$. Such an orbit exists if there is no singularity separating the fixed points in the phase space and the upstream fixed point is unstable and the downstream fixed point is

stable. However, singularities exist when the coefficient $D(H, We, c)$ of $H_{\xi\xi\xi}$ in (42) vanishes. In the phase space, these singularities are infinite planes normal to the H -axis. The phase trajectories, near the singular planes are led to

infinities and cannot therefore flow across these singularities. One of these singular planes is $H_s^{(0)}=0$, which corresponds physically to a dry bed. The other singularity planes are given by

$$\left. \begin{matrix} H_s^{(1)} \\ H_s^{(2)} \end{matrix} \right\} = \frac{We + \frac{1211}{3360}c(c-1) \pm \left\{ \left(We + \frac{1211}{3360}c(c-1) \right)^2 - \left(\frac{391}{1680}c^2 \right) \left(\frac{241}{448}(1-c)^2 \right) \right\}^{1/2}}{\left(\frac{391}{3360}c^2 \right)} \quad (46)$$

In the We versus c plane, the parameter regions where none of the singular planes lie between H_I and H_{II} in the phase space are found from the trajectories

$$D_1(c, We) = We - \frac{99}{210}c^2 + \frac{601}{840}c - \frac{241}{448} = 0, \quad (47)$$

which gives the points of intersection between H_I and $H_s^{(1)}$ (or $H_s^{(2)}$) (the solid curve in Fig. 4) and from the trajectories

$$D_2(c, We) = \frac{-We}{2} - \frac{391}{6720}c^3 - \frac{3087}{4480}c^2 + \frac{8441}{6720}c - \frac{241}{448} + \left(\frac{We}{2} + \frac{2813}{13440}c^2 - \frac{1211}{6720}c \right) \sqrt{4c-3} = 0, \quad (48)$$

which gives the points of intersection between H_{II} and $H_s^{(1)}$ (or $H_s^{(2)}$) (the dashed curve in Fig. 4).

Figure 4 shows these singularity boundaries and in the shaded regions, heteroclinic orbits are possible, where the singular planes do not lie between the two fixed points.

B. Search for oscillatory orbits emerging from a limit cycle around the fixed point

It is also of interest to anticipate another type of continuous orbit in certain parts of $\cot \theta/Re$ versus c plane. This

motivates the search for the Hopf bifurcation threshold which marks the first appearance of limit cycles or periodic solutions. Such a threshold occurs when the fixed point possesses a pair of purely imaginary eigenvalues and a negative real eigenvalue. This requires the knowledge of the eigenvalue properties of the two fixed points H_I and H_{II} in each of the following four regimes: (i) $We > We^{(1)}$ ($=0.60742$); (ii) $We^{(2)}$ ($=0.513$) $< We < We^{(1)}$; (iii) $We^{(3)}$ ($=0.03182$) $< We < We^{(2)}$; and (iv) $0 < We < We^{(3)}$, determined by their relative positions of the singularity branches (Fig. 5).

In order to determine the possible bifurcations of the fixed points as they become unstable, small perturbations around the fixed points are considered so that $\mathbf{H} = \mathbf{H}^* + \mathbf{h}$, where \mathbf{H}^* denotes one of the two fixed points H_I or H_{II} and \mathbf{h} is the perturbation. The linearized system obtained from (43) is given by

$$\frac{d\mathbf{h}}{d\xi} = \mathbf{J}\mathbf{h}, \quad \mathbf{J} = \begin{pmatrix} 0 & 1 & 0 \\ 0 & 0 & 1 \\ -\beta_3/Re & -\beta_2 & -\beta_1/Re \end{pmatrix}, \quad (49)$$

where

$$\left. \begin{matrix} \beta_1 = \frac{\{-\frac{9}{5}cH^2 - \frac{36}{5}H(1-c)\}}{WeH^3 - \frac{391}{6720}c^2H^4 + \frac{1211}{3360}c(c-1)H^3 - \frac{241}{448}(c-1)^2H^2}, \\ \beta_2 = \frac{\left\{ -\frac{6}{35}c^2H^2 + \frac{6}{35}c(1-c)H + \frac{54}{35}(1-c)^2 - \frac{3 \cot \theta}{Re} \right\}}{WeH^3 - \frac{391}{6720}c^2H^4 + \frac{1211}{3360}c(c-1)H^3 - \frac{241}{448}(c-1)^2H^2}, \\ \beta_3 = \frac{\{3(3H^2 - c)\}}{WeH^3 - \frac{391}{6720}c^2H^4 + \frac{1211}{3360}c(c-1)H^3 - \frac{241}{448}(c-1)^2H^2} \end{matrix} \right\}_{H=H_I; H=H_{II}} \quad (50)$$

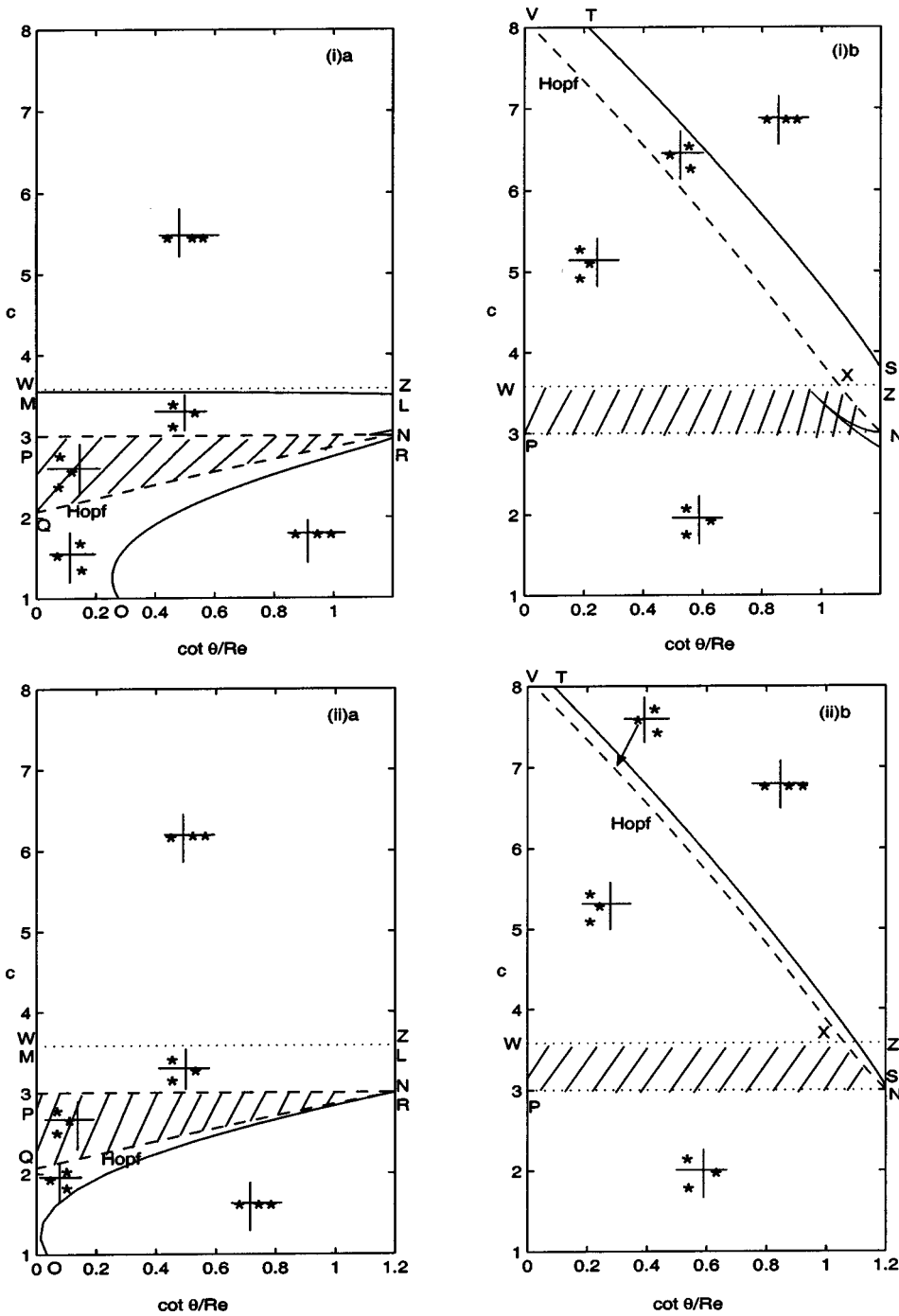


FIG. 5. Eigenvalue behavior of the two fixed points in the c versus $\cot \theta/Re$ plane for $We=1$ and (i) $Re = 1/0.075 \approx 13.33$; (ii) $Re=100$. (a) H_I ; (b) H_{II} .

The characteristic equation for the eigenvalue λ of the Jacobian matrix J is given by

$$\lambda^3 + \frac{\beta_1}{Re} \lambda^2 + \beta_2 \lambda + \frac{\beta_3}{Re} = 0. \tag{51}$$

The eigenvalues in terms of the small parameter $1/Re$ are given by

$$\begin{aligned} \lambda_1 &= -\frac{1}{Re} \frac{\beta_3}{\beta_2} + o(Re^{-2}), \\ \lambda_{2,3} &= \frac{1}{Re} \frac{\beta_3 - \beta_1 \beta_2}{2\beta_2} \pm i\sqrt{\beta_2} + o(Re^{-2}). \end{aligned} \tag{52}$$

If at a fixed point $\beta_2 > 0$, then λ_2 and λ_3 are complex and the fixed point is a saddle-spiral and if $\beta_2 < 0$, then λ_2 and λ_3 are real and the fixed point is a saddle node. The zeros of β_2 represent the boundaries of eigenvalue behavior between saddle-spirals and saddle-nodes.

In the parameter space $(We, Re, \cot \theta, c)$, the Hopf-bifurcation thresholds separate eigenvalues $\lambda_1 < 0$, Real part of $(\lambda_2, \lambda_3) > 0$ from those of $\lambda_1 < 0$, Real part of $(\lambda_2, \lambda_3) < 0$. The conditions for the Hopf-bifurcation threshold are obtained from (52) as

$$\beta_1 \beta_2 = \beta_3, \quad \beta_1 > 0, \quad \beta_2 > 0, \tag{53}$$

which ensure that the real eigenvalue λ_1 is negative and that

TABLE I. Hopf-bifurcation thresholds for the fixed points.

Range of Weber number	Regime H_I	Regime H_{II}	Typical value chosen
1. $We > We^{(1)}$	$0 \leq \frac{\cot \theta}{Re} < 1.2$	$0 \leq \frac{\cot \theta}{Re} < 1.2$	$We = 5$
2. $We^{(2)} < We < We^{(1)}$	$0 \leq \frac{\cot \theta}{Re} < 1.2$	$0 \leq \frac{\cot \theta}{Re} \leq 0.72029$ $1.14072 \leq \frac{\cot \theta}{Re} < 1.2$	$We = 0.55$
3. $We^{(3)} < We < We^{(2)}$	$0 \leq \frac{\cot \theta}{Re} \leq 0.7549$	$0 \leq \frac{\cot \theta}{Re} \leq 0.372733$	$We = 0.3$

a pair of complex eigenvalues exist. Table I shows that for a Hopf bifurcation to occur at any fixed $\cot \theta/Re$, it is necessary that the Weber number exceeds a certain minimum value. The boundary separating saddle spirals from saddle nodes corresponds to the double root of the characteristic equation (51), which occurs at

$$\left(\frac{2\beta_1^2}{Re^2} - 6\beta_2\right) \left(2\beta_2^2 - \frac{6\beta_1\beta_2}{Re^2}\right) - \left(\frac{\beta_1\beta_2}{Re} - \frac{9\beta_3}{Re}\right)^2 = 0. \tag{54}$$

The eigenvalue properties of the two fixed points are displayed in Figs. 5(i)a and 5(i)b for the case $We=1$, $Re=1/0.075 \approx 13.33$, in the regime of instability $0 \leq \cot \theta/Re < 1.2$. The Hopf-bifurcation thresholds are shown by QN and VN. PN is the transcritical bifurcation boundary ($c=3$), ML and OR are the boundaries dividing the saddle nodes for the fixed point H_I . For the fixed point H_{II} , TS is such a boundary. The qualitative properties of the eigenvalues are indicated by their locations in the complex plane. WZ is the singularity boundary ($D_1=0$ for H_I). Table II presents the

eigenvalue properties of the fixed points and possible orbits in the phase space for $Re=13.33$, $We=1$ in the $\cot \theta/Re$ versus c plane.

The eigenvalue behavior of the two fixed points for $Re=100$, $We=1$ are presented in Figs. 5(ii)a, 5(ii)b. It is noted that at this large Reynolds number the regions of saddle node or stable node in the neighborhood of neutral stability shrink in size. The conclusions for $Re=13.33$ are applicable also for $Re=100$ and the qualitative trend continues for still higher Reynolds numbers. Moving near or away from the singularities, the region of heteroclinic orbits and the span of Hopf-bifurcation thresholds in the linearly unstable region, shrink or expand when the Weber number is decreased or increased. In the next section, results based on the numerical integration of the third order dynamical system (43) are presented.

V. BIFURCATION SCENARIOS: NUMERICAL SOLUTION

By continuously varying the transcritical bifurcation parameter c about $c=3$, either heteroclinic orbits or other non-

TABLE II. Eigenvalue properties and possible orbits in phase space for $We=1$, $Re=13.33$ (Fig. 5).

	H_I	H_{II}	Possible orbit in phase space
Region PNQ ($c < 3$)	$\lambda_1 < 0$, $Real(\lambda_2, \lambda_3) < 0$ stable saddle-spiral (PJKNQ) (or) stable node (JKN) ($\lambda_1, \lambda_2, \lambda_3 < 0$)	Saddle spiral with stable plane focus $\lambda_1 > 0$, $Real(\lambda_2, \lambda_3) < 0$ (or) saddle node with stable plane focus ($\lambda_1 > 0, \lambda_2, \lambda_3 < 0$)	Heteroclinic orbit from H_{II} to H_I
Region bounded by QN and OR ($c < 3$)	Is unstable	Is unstable	Bifurcate supercritically to a limit cycle
Region WXNP ($c > 3$)	Unstable saddle spiral with stable plane focus (or) a saddle-node with stable plane focus	A stable saddle-spiral (or) a stable saddle-node	Heteroclinic orbit from H_I to H_{II}
Region VXW ($c > 3$)	Is unstable	Is stable	No heteroclinic orbit, since H_I and H_{II} are separated by a singular plane WZ
XNZ in the region VNST ($c > 3$)			Attractors if any, bifurcate from H_{II} and are connected to H_I

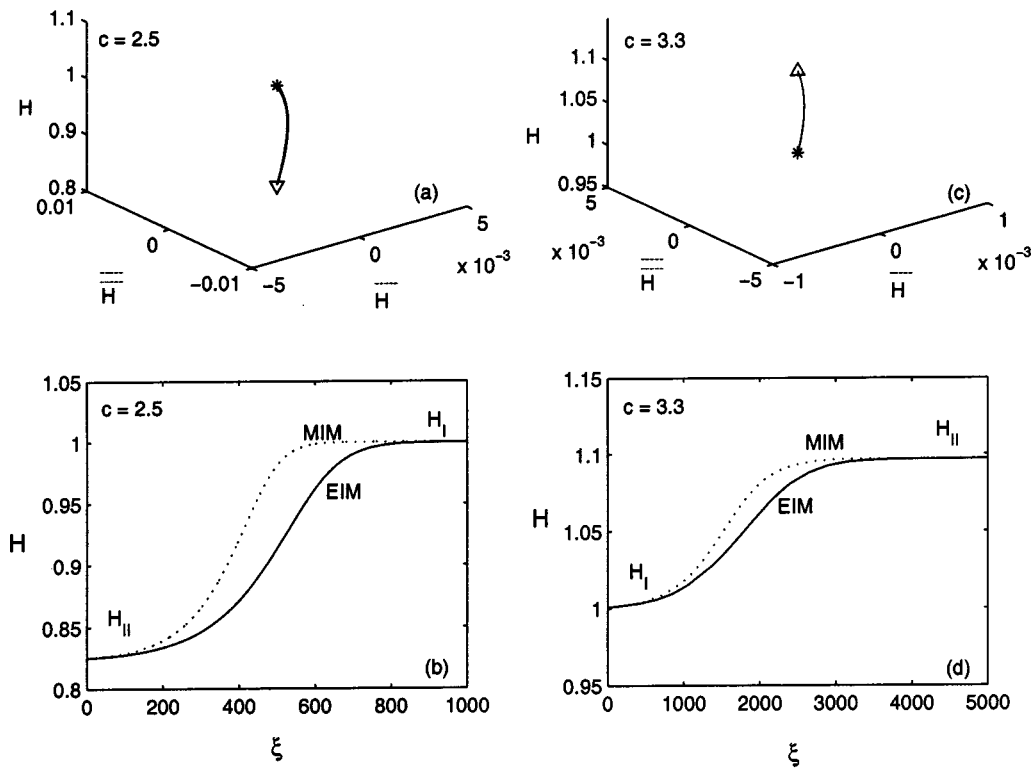


FIG. 6. A heteroclinic orbit, H_{II} to H_I (a), (b), H_I to H_{II} (c), (d), for $We=1$, $Re=100$, $\cot \theta/Re=0.4$ (a), (c) The phase trajectory; (b), (d) the profile.

linear attractors are obtained for each fixed value of We , $\cot \theta/Re$ ($We \leq 10$ and $Re=13.33$ and 100). No nonlinear attractor has been found in the regime of linear stability, $\cot \theta/Re \geq 1.2$ for any Weber number and Reynolds number. In the linear regime of instability, the three dimensional dynamical system is solved numerically using ODE15s which is available in MATLAB5.3 with bounds for relative error as 10^{-10} . ODE15s in MATLAB is a variable order solver based on the numerical differentiation formulas. Optionally, it uses the backward differentiation formulas, also known as Gear's method. It is a multistep solver.

A. Heteroclinic orbits

For a typical value of wave speed $c=2.5$, which lies above the Hopf threshold for H_I but below $c=3.0$, there is a heteroclinic orbit from H_{II} to H_I and its phase portrait, wave profile are given in Figs. 6(a) and 6(b). For any c above 3.0, which lies below the singularity boundary, there is a heteroclinic orbit from H_I to H_{II} and the phase portrait, wave profile are presented in Figs. 6(c) and 6(d). Figure 6 also shows the corresponding results obtained by MIM.

When c is slightly decreased from the Hopf bifurcation threshold, supercritical Hopf bifurcation occurs for the first fixed point. In this case, integration is carried out by taking the initial phase point in the neighborhood of this attractor and its subsequent bifurcation is then pursued. The computation is terminated at the point where no attractor could be detected. Integration is carried out for sufficiently long time until the trajectories finally settle down on the attractor. Following Lee and Mei,⁴⁵ the bifurcation diagram for the permanent wave is obtained by choosing all the local maxima

H_m of the time series for the flow depth H as the representative points and they are plotted against the bifurcation parameter c . In this bifurcation diagram, a single representative point denotes a limit cycle, two points at different heights denote a period-2 limit cycle and so on.

B. Summary of bifurcation scenarios for $Re \approx 13.33$ and $Re=100$

The results of the numerical experiment show four different types of bifurcation scenarios. Typical bifurcation sequences for $We=1$ for a set of values of $\cot \theta/Re$ have been presented in the following figures.

- (1) Simple homoclinic bifurcation from the primary flow H_I [$\cot \theta/Re=0.9$; Figs. 7(a), 8(i)a, 8(i)b].
- (2) A period-doubling followed by a simple homoclinic bifurcation from the primary flow H_I [$\cot \theta/Re=0.55$; Figs. 7(b), 8(ii)a, 8(ii)b].
- (3) Multiple hump homoclinic bifurcation from the primary flow H_I [$\cot \theta/Re=0.48$; Figs. 7(c), 8(iii)a, 8(iii)b].
- (4) Dominant scenario of period-doubling bifurcation leading to chaos from the primary flow H_I [$\cot \theta/Re=0$; Figs. 7(d), 8(iv)a, 8(iv)b].

The bifurcation scenarios have been numerically determined for a wide range of Weber numbers, $We \leq 10$, in order to facilitate a comparison with the results obtained by Lee and Mei⁴⁵ using MIM. The boundaries separating regimes of different bifurcation scenarios in terms of $\cot \theta/Re$ in the regime of linear instability in the We versus $\cot \theta/Re$ plane

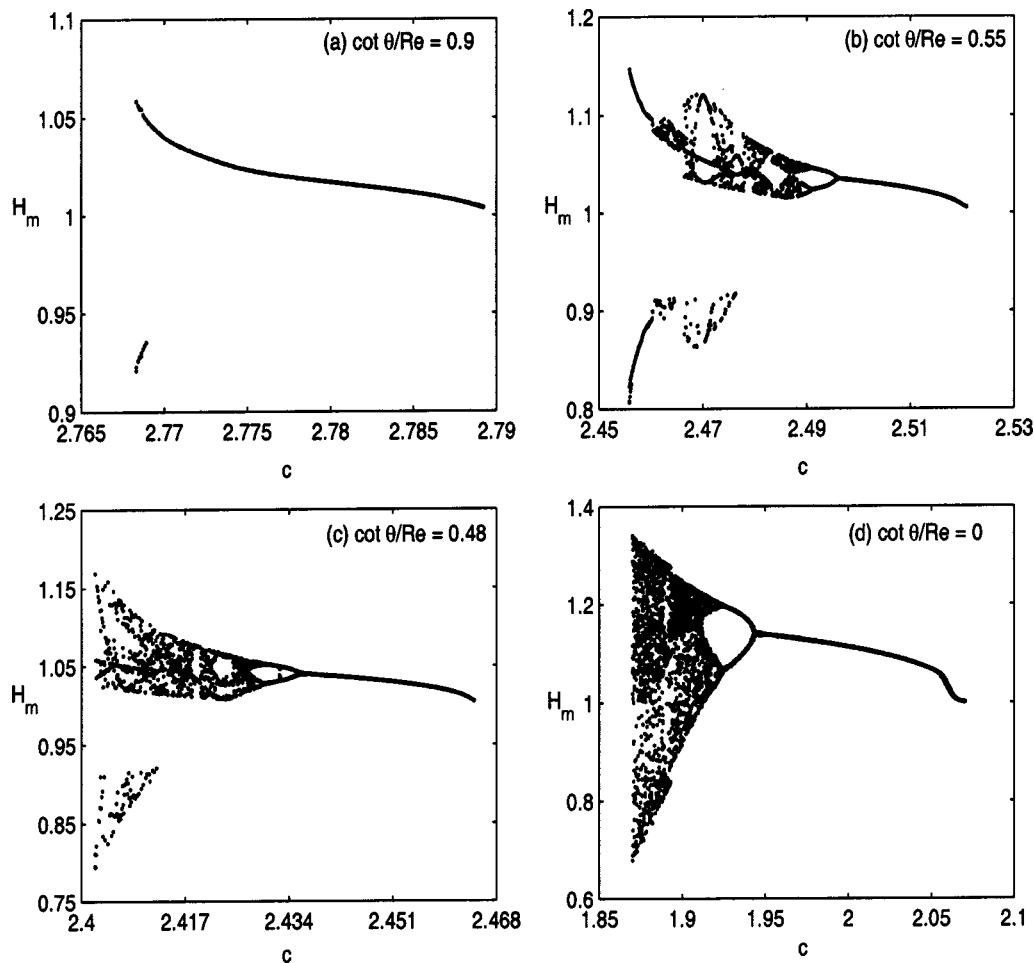


FIG. 7. The bifurcation diagrams of limit cycles from H_I : $We=1$, $Re=1/0.075 \approx 13.33$. (a) Simple homoclinic bifurcation; (b) period-doublings+ simple homoclinic bifurcation, (c) three hump homoclinic bifurcation, (d) period-doubling route to chaos.

are presented in Figs. 9 and 10 for limit cycles from H_I for the cases $Re=13.33$ and $Re=100$ using MIM [Figs. 9(a), 10(a)] and EIM [Figs. 9(b), 10(b)].

It is observed from Fig. 9(b) (results obtained by EIM) that for $Re=13.33$, the Hopf-bifurcation threshold extends throughout the entire regime of linear instability for $We > We^{(2)} (=0.513)$. In this region, the limit cycle either undergoes homoclinic bifurcations or period-doubling bifurcations. The region in which homoclinic bifurcations are observed dominates for smaller values of Weber numbers and this region has spread to the entire regime of linear instability around $We = We^{(2)} = 0.513$. The period-doubling bifurcations exist for large Weber numbers. As the threshold for linear instability predicted by EIM is $0 \leq \cot \theta/Re < 1.2$ (as compared to that predicted by MIM as $0 \leq \cot \theta/Re < 1$), the region in which the Hopf-bifurcation threshold prevails is larger than that in Fig. 9(a).

For $We < We^{(2)}$, a Hopf-bifurcation threshold exists and the limit cycle undergoes period-doubling bifurcations for small values of $\cot \theta/Re$. As We is further reduced, the limit cycles are the only attractors.

When $Re=100$ [Fig. 10(b)], the homoclinic regime lies close to the linear instability threshold in $We > We^{(2)}$, the limit cycle regime has diminished and lies close to the

boundary of no attractor region in $We < We^{(2)}$.

Bifurcation scenarios presented in Figs. 9 ($Re=13.33$) and 10 ($Re=100$) for bifurcations from the primary flow H_I clearly show the differences in quantitative predictions by the two models, although qualitatively similar scenarios are observed in the respective regions. In view of qualitatively similar predictions of the bifurcation scenarios by both the methods, the bifurcation scenarios obtained for bifurcations from the primary flow H_{II} for $Re=13.33$ and $Re=100$ are not presented here. However, as in the earlier case, quantitative predictions by EIM are different from that by MIM.

VI. COMPARISON WITH EXPERIMENTS

Experimental data are very scarce in the literature for free falling films and the experimental results available to date are mostly for high surface tension fluids, in which the wave amplitude is relatively small compared to the mean film thickness.^{1,15,53,57,58} Experimental results by Liu and Gollub^{52,59} using glycerin solutions are mostly confined to small amplitude waves near the neutral curve. Further, nearly all available experimental data on amplitude, speed and wavelength of nearly periodic finite-amplitude waves are only for falling water films along vertical circular cylinders

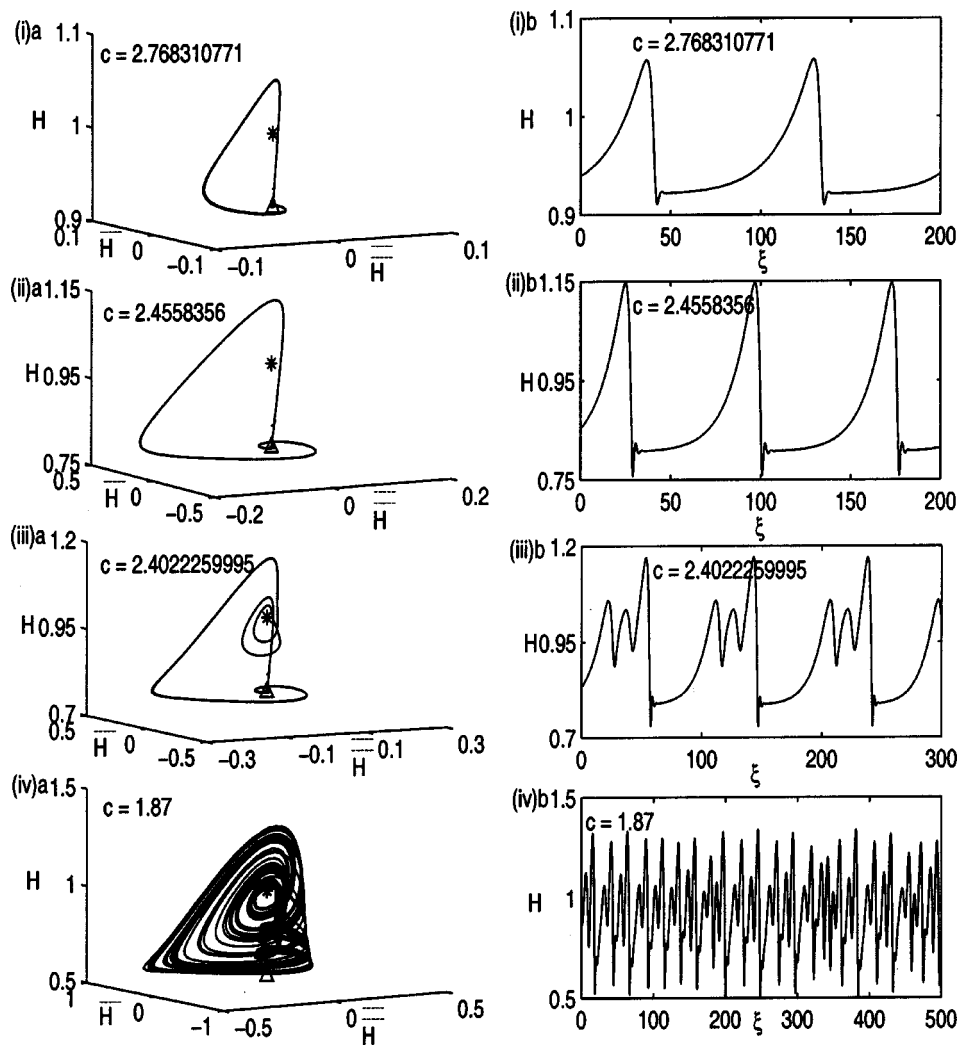


FIG. 8. Selected phase portraits (a) and corresponding wave profiles (b) of attractors during (i) simple homoclinic bifurcation; $\cot \theta/\text{Re}=0.9$; (ii) period-doublings+ simple homoclinic bifurcation; $\cot \theta/\text{Re}=0.55$; (iii) three hump homoclinic bifurcation; $\cot \theta/\text{Re}=0.48$, (iv) period-doubling route to chaos; $\cot \theta/\text{Re}=0$ for $\text{We}=1$, $\text{Re}=1/0.075 \approx 13.33$ from H_1 .

of limited length. Therefore, precise comparisons of the present theory which corresponds to the asymptotic range of large time for films on a plane with the observations on a cylindrical geometry are difficult. In addition, the present theory is strictly valid for $\text{We} \approx O(1)$, whereas in the experiments mentioned above, the effect of surface tension is strong so that $\text{We} > 20$.

Most of the reported works on a direct numerical solution of Navier–Stokes equations are restricted to flow with relatively small Reynolds numbers. For instance, Bach and Villadsen⁶⁰ have solved the transient Navier–Stokes equations in the Lagrangian coordinates by the finite-element method for vertically falling flows with $2.5 < \text{Re} < 25$. Khesghi and Scriven⁶¹ have obtained periodic and solitary wave solutions for Navier–Stokes equations on a vertical plate with $\text{Re} < 10$.

Salamon *et al.*⁶² have constructed periodic and solitary waves down a vertical plate, by transforming the Navier–Stokes equations to a constant moving coordinate and searching for permanent waves by finite elements. Their solutions have compared favorably well with the experimental results of Kapitza and Kapitza¹ on a circular cylinder and the numerical simulations reported by Ho and Patera.⁶³ Their solution branches on the wave number–wave speed param-

eter plane are similar to those reported by Chang *et al.*¹⁹ at an infinitely long wave limit. They have presented (Figs. 8 and 11; Salamon *et al.*⁶²) the wave speed c as a function of Reynolds number Re for traveling wave solutions computed with the finite element method and have compared with the long-wave evolution equation solutions for Reynolds number ranging from 0 to 10 and Weber number $\text{We} = 1000$ and 76.4 , respectively.

Further, it is worth mentioning here that Chang and Demekhin⁴⁴ (Fig. 3.5, p. 60, Chap. 3) have presented a comparison of various models obtained using a combination of Galerkin–Petrov method with weighted residuals with other available models in the literature and have presented the speed of the primary solitary wave (at the end of the primary periodic wave family–pulse solution) as a function of the Reynolds number for a fixed Kapitza number of 252. They have chosen the wave speed of this solitary wave as a measure of comparison among various models, as this solitary wave is the most dominant wave (stable) that can be observed on any falling film and therefore its speed can be measured very precisely. Based on the pulse solutions of these models for vertically falling films, the speed and amplitude of one-hump solitary waves have been presented for Reynolds number ranging from 0 to 8 (small Reynolds num-

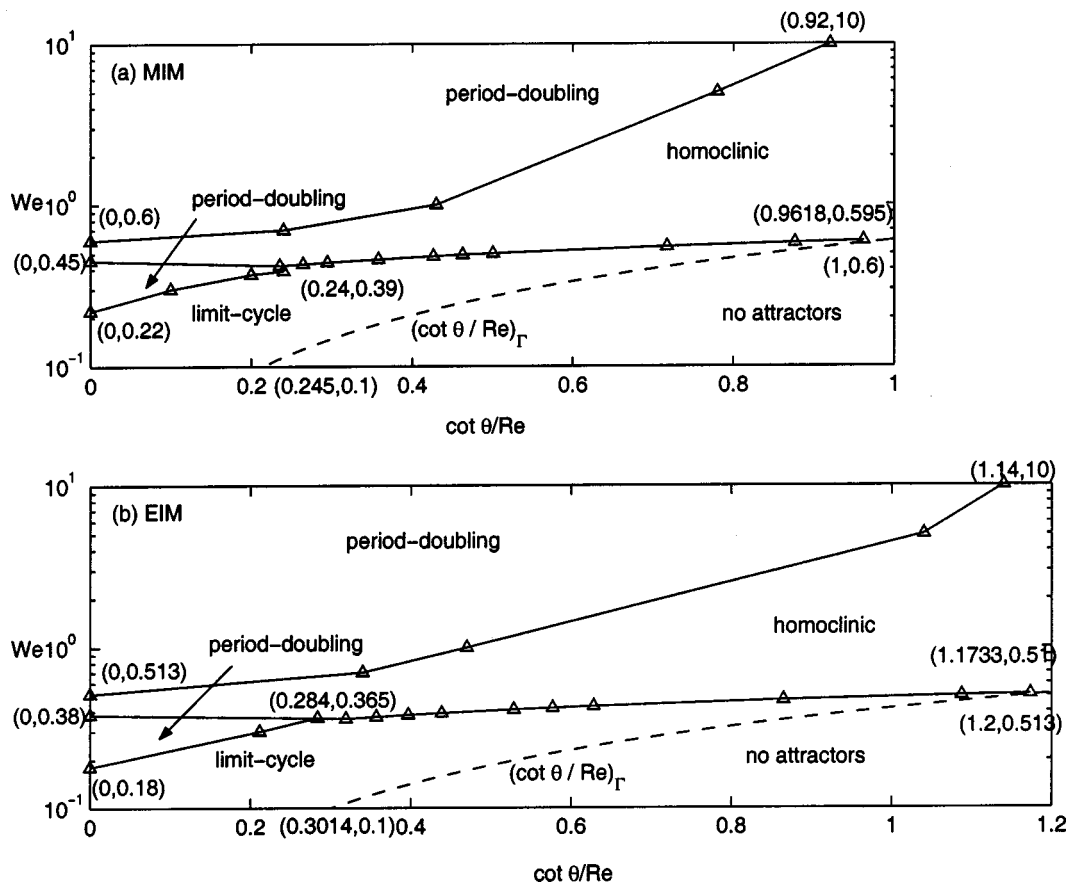


FIG. 9. Bifurcation scenarios delimited in the regime of linear SW instability in the We versus $\cot \theta / Re$ plane for limit cycles from H_1 for $Re=1/0.075 \approx 13.33$.

ber) and Kapitza number 252 (Weber number ranging from 363.44689 to 11.3577).

As the present investigation is for large Reynolds numbers $Re \approx O(\epsilon^{-1})$ and small to moderate surface tension $We \approx O(1)$, the present results should complement the above existing theories on large Reynolds number flows $Re \approx O(\epsilon^{-1})$ with strong surface tension $We \approx O(\epsilon^{-2})$ as well as theories for small Reynolds number flows $Re \approx O(1)$ with either strong surface tension $We \approx O(\epsilon^{-2})$ or weak surface tension $We \approx O(1)$.

With the constraints mentioned above, the numerical predictions of the present nonlinear theory and the experiments of Yu *et al.*⁴⁹ for chaotic large amplitude waves on flows of aqueous solutions with Kapitza number $Ka=3550$ are presented in Fig. 11. The numerical results correspond to the highest period-1 waves taken at the threshold where the first fixed point H_1 bifurcates to a period-2 limit cycle for each Reynolds number. Though conducted on a circular tube of finite radius, Yu's data are relevant in the present context ($50 < Re < 300$, $0.3 < We < 7$).

Although experimental data on vertically falling films presented by Chu and Duckler^{46,47} in terms of statistical properties may be used for chaotic waves of large amplitude sufficiently downstream, they are not relevant for a comparison with the present theory. The Weber numbers in their analysis are too small ($\ll 0.1$) and are outside the range of validity of the present theory. Figure 11 shows the wave

propagation speed as a function of Reynolds numbers. Theoretical predictions of Hopf thresholds and the limiting speed for chaotic waves from the present numerical results and the results from momentum integral method along with those of Yu *et al.*⁴⁹ are presented. The wave speeds obtained from the experiments lie in general above the Hopf threshold of Yu *et al.*⁴⁹ On the other hand, they fall in between the Hopf thresholds and limiting speeds predicted by the present theory (EIM) as well as MIM. It is observed that the theoretical predictions follow the same trend that is observed in experiments.

VII. CONCLUSION

The finite amplitude waves of stationary form on a thin viscous film down an inclined plane at high Reynolds numbers and moderate Weber numbers have been considered using the energy integral method (EIM). The two equation model obtained using EIM reduces to a third order dynamical system in the frame of reference moving with the steady wave speed. Through numerical integration of the dynamical system, complex bifurcation scenarios have been captured and the results clearly show the quantitative differences in the predictions by EIM and MIM, although the qualitative predictions are similar. The analysis in Sec. III shows that the regime of linear instability predicted by EIM is $0 \leq \cot \theta / Re < 6/5$ whereas it is predicted as $0 \leq \cot \theta / Re < 1$ by MIM. The

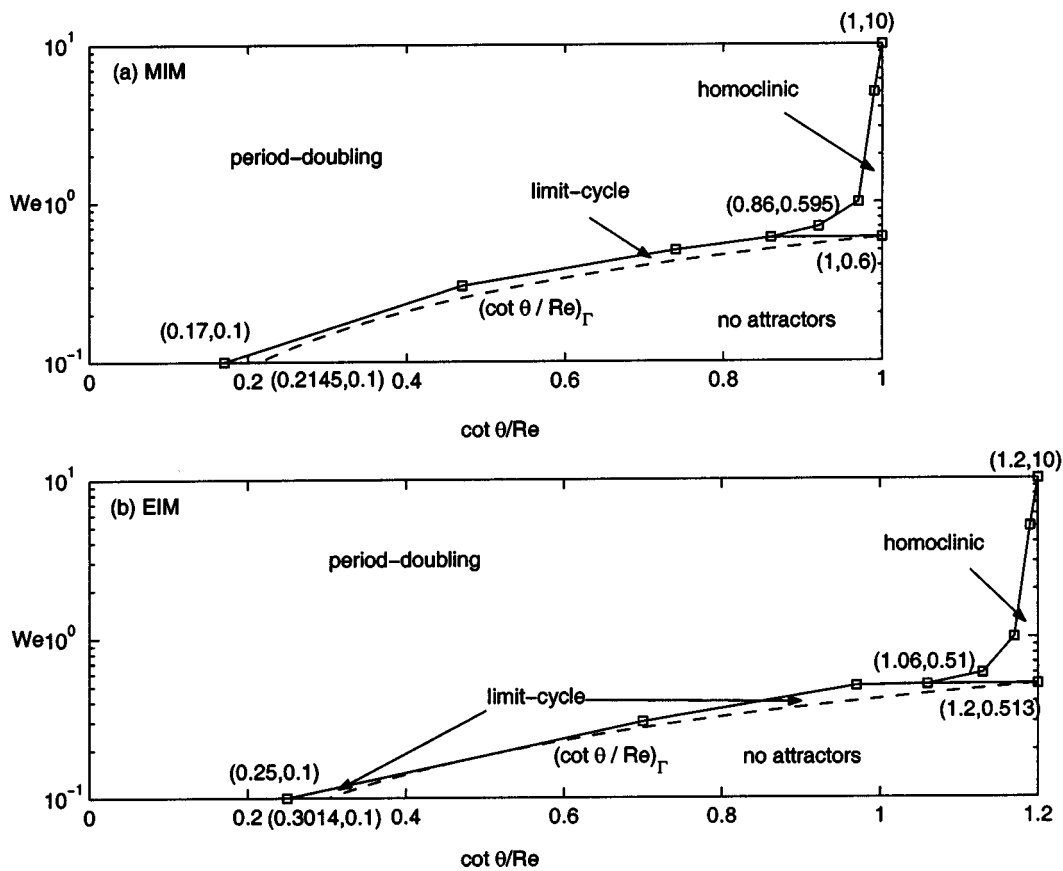


FIG. 10. Bifurcation scenarios delimited in the regime of linear SW instability in the We versus $\cot \theta / Re$ plane for limit cycles from H_1 for $Re=100$.

linear instability threshold predicted by EIM is identical to that predicted by the classical result of an Orr–Sommerfeld analysis for small Reynolds number flows by Benjamin⁵⁰ and Yih⁵¹ and the experimental verification by Liu and Gollub.⁵²

The results of the linear instability of uniform flow show that the new model can describe the dynamics of wave evolution on falling films for Re up to 100.

The analysis in Sec. V demonstrates that the present

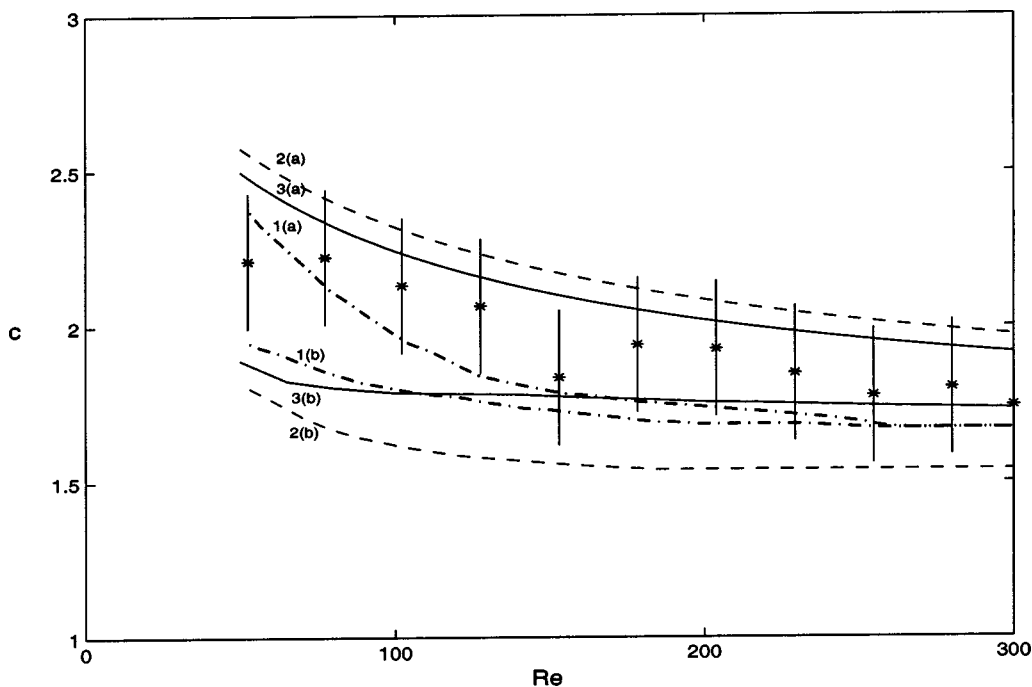


FIG. 11. A comparison of the Hopf-bifurcation threshold and limiting speed of chaotic waves. 1. Theory of Yu *et al.* (Ref. 49); 2. Theory of Lee and Mei (Ref. 45); 3. Present theory; *—experiment of Yu *et al.* (Ref. 49); (a) Hopf-bifurcation threshold; (b) limiting speed of chaotic waves.

model also captures the different dynamical phenomena exhibited by MIM. Although both the methods exhibit similar bifurcation scenarios, there are quantitative differences (as is evident from numerical integration results). Although definitive comparisons with the available experiments cannot be made due to reasons stated in Sec. VI, the results of the most relevant experimental predictions show that the present model results follow the same trend that is observed in experiments. Therefore, the present approach (EIM) (i) shows another way of simplifying Navier–Stokes equations for the film flow system down an inclined plane and (ii) can be regarded as a reasonable alternative to the more classical approach using MIM.

ACKNOWLEDGMENTS

We sincerely thank Professor L. Gary Leal, Editor, and the two referees for their very valuable comments and suggestions. These have helped us a lot in improving the quality, content and style of the paper.

- ¹P. L. Kapitza and S. P. Kapitza, “Wave flow of thin layers of a viscous fluid,” *Zh. Eksp. Teor. Fiz.* **19**, 105 (1949).
- ²D. J. Benney, “Long waves on liquid film,” *J. Math. Phys. (Cambridge, Mass.)* **45**, 150 (1966).
- ³S. P. Lin, “Finite-amplitude stability of a parallel flow with a free surface,” *J. Fluid Mech.* **36**, 113 (1969).
- ⁴B. Gjevik, “Occurrence of finite amplitude surface waves on falling liquid films,” *Phys. Fluids* **13**, 1918 (1970).
- ⁵B. Gjevik, “Spatially varying finite-amplitude wave trains on falling liquid films,” *Acta Polytech. Scand., Mech. Eng. Ser.* **61**, 1 (1971).
- ⁶C. Nakaya, “Long waves on a thin fluid layer flowing down an inclined plane,” *Phys. Fluids* **18**, 1407 (1975).
- ⁷C. Nakaya, “Stationary waves on a viscous fluid film down a vertical wall,” *J. Phys. Soc. Jpn.* **50**, 2795 (1981).
- ⁸A. Pumir, A. Manneville, and Y. Pomeau, “On solitary waves running down an inclined plane,” *J. Fluid Mech.* **135**, 27 (1983).
- ⁹H.-C. Chang, “Travelling waves on fluid interfaces: Normal form analysis of the Kuramoto–Sivashinsky equation,” *Phys. Fluids* **29**, 3142 (1986).
- ¹⁰H.-C. Chang, “Onset of nonlinear waves on falling films,” *Phys. Fluids A* **1**, 1314 (1989).
- ¹¹S. W. Joo, S. H. Davis, and S. G. Bankoff, “Long-wave instabilities of heated falling films: two-dimensional theory of uniform layers,” *J. Fluid Mech.* **230**, 117 (1991).
- ¹²V. Ya. Shkadov, “Wave conditions in the flow of thin layer of a viscous liquid under the action of gravity,” *Izv. Akad. Nauk SSSR, Mekh. Zhidk. Gaza* **1**, 43 (1967).
- ¹³V. Ya. Shkadov, “Theory of wave flows of a thin layer of a viscous liquid,” *Izv. Akad. Nauk SSSR, Mekh. Zhidk. Gaza* **2**, 20 (1968).
- ¹⁴J. Lee, “Kapitza’s method of film flow description,” *Chem. Eng. Sci.* **24**, 1309 (1969).
- ¹⁵S. V. Alekseenko, V. Y. Nakoryakov, and B. G. Pokusaev, “Wave formation on vertical falling liquid films,” *AIChE J.* **31**, 1446 (1985).
- ¹⁶T. Prokopiou, M. Cheng, and H.-C. Chang, “Long waves on inclined films at high Reynolds numbers,” *J. Fluid Mech.* **222**, 665 (1991).
- ¹⁷Yu. Ya. Trifonov and O. Yu. Tsvetodub, “Nonlinear waves on the surface of a falling liquid film. I,” *J. Fluid Mech.* **229**, 531 (1991).
- ¹⁸Yu. Ya. Trifonov and O. Yu. Tsvetodub, “Nonlinear waves on the surface of a falling liquid film. II,” *J. Fluid Mech.* **244**, 149 (1992).
- ¹⁹H.-C. Chang, E. A. Demekhin, and D. I. Kopelevich, “Nonlinear evolution of waves on a vertically falling film,” *J. Fluid Mech.* **250**, 433 (1993).
- ²⁰H. I. Andersson and F. Irgens, “Hydrodynamic entrance length of non-Newtonian liquid films,” *Chem. Eng. Sci.* **45**, 537 (1990).
- ²¹H. I. Andersson, “On integral method predictions of laminar film flow,” *Chem. Eng. Sci.* **39**, 1005 (1984).
- ²²H. I. Andersson and F. Irgens, “Gravity-driven laminar film flow of power-law fluids along vertical walls,” *J. Non-Newtonian Fluid Mech.* **27**, 153 (1988).
- ²³H. I. Andersson and F. Irgens, “Film flow of power-law fluids,” in *Encyclopedia of Fluid Mechanics*, edited by N. P. Cheremisinoff (Gulf, Houston, 1990), Vol. 9, p. 617.
- ²⁴H. I. Andersson and T. Ytrehus, “Falkner–Skan solution for gravity-driven film flow,” *ASME J. Appl. Mech.* **52**, 457 (1985).
- ²⁵H. I. Andersson and D.-Y. Shang, “An extended study of the hydrodynamics of gravity-driven film flow of power-law fluids,” *Fluid Dyn. Res.* **22**, 345 (1998).
- ²⁶A. Stücheli and M. N. Özisik, “Hydrodynamic entrance lengths of laminar falling films,” *Chem. Eng. Sci.* **31**, 369 (1976).
- ²⁷M. N. Tekic, D. Posarac, and D. Petrovic, “A note on the entrance region lengths of non-Newtonian laminar falling films,” *Chem. Eng. Sci.* **41**, 3230 (1986).
- ²⁸H. I. Andersson, “Numerical solutions of a TSL-model for free surface flows,” *Notes on Numerical Fluid Mechanics*, Proceedings of the 5th GAMM-Conference on Numerical Methods in Fluid Mechanics, 1984, Vol. 7, p. 9.
- ²⁹S. H. Crandall and A. El-Shafei, “Momentum and energy approximations for elementary squeeze film damper flows,” *ASME Trans. J. Appl. Mech.* **60**, 728 (1993).
- ³⁰A. F. Elkouh, “Inertia effect in laminar radial flow between parallel plates,” *Int. J. Mech. Sci.* **9**, 253 (1967).
- ³¹A. F. Elkouh, “Fluid inertia effects in non-Newtonian squeeze films,” *ASME J. Lubr. Technol.* **98**, 409 (1976).
- ³²D. C. Kuzma, “Fluid inertia effects in squeeze films,” *Appl. Sci. Res.* **18**, 15 (1967).
- ³³V. K. Kapur and K. Verma, “Energy integral approach for MHD hydrostatic thrust bearings,” *ASME J. Lubr. Technol.* **97**, 647 (1975).
- ³⁴S. R. Turns, “Annular squeeze films with inertial effects,” *ASME J. Lubr. Technol.* **105**, 381 (1983).
- ³⁵Y. Han and R. J. Rogers, “Squeeze film force modeling for large amplitude motion using an elliptical velocity profile,” *Trans. ASME, J. Tribol.* **118**, 687 (1996).
- ³⁶R. Usha and P. Vimala, “Squeeze film force using an elliptical velocity profile,” *ASME Trans. J. Appl. Mech.* **70**, 137 (2003).
- ³⁷J. A. Tichy and W. O. Winer, “Inertial considerations in parallel circular squeeze film bearings,” *ASME J. Lubr. Technol.* **92**, 588 (1970).
- ³⁸R. J. Grimm, “Squeezing flows of Newtonian liquid films—An analysis including fluid inertia,” *Appl. Sci. Res.* **32**, 149 (1976).
- ³⁹A. El-Shafei, “Dynamics of rotors incorporating squeeze film dampers,” Ph.D. thesis, Department of Mechanical Engineering, Massachusetts Institute of Technology, Cambridge, MA, 1988.
- ⁴⁰H. Esmonde, J. A. Fitzpatrick, H. J. Rice, and F. Axisa, “Modelling and identification of nonlinear squeeze film dynamics,” *J. Fluids Struct.* **6**, 223 (1992).
- ⁴¹L. T. Nguyen and V. Balakotaiah, “Modeling and experimental studies of wave evolution on free falling viscous films,” *Phys. Fluids* **12**, 2236 (2000).
- ⁴²T. Ooshida, “Surface equation of falling film flows with moderate Reynolds number and large but finite Weber number,” *Phys. Fluids* **11**, 3247 (1999).
- ⁴³C. Ruyer-Quil and P. Manneville, “Modeling film flows down inclined planes,” *Eur. J. Biochem.* **6**, 277 (1998).
- ⁴⁴H.-C. Chang and E. A. Demekhin, *Complex Wave Dynamics on Thin Films* (Elsevier Applied Science, Amsterdam, 2002).
- ⁴⁵J. J. Lee and C. C. Mei, “Stationary waves on an inclined sheet of viscous fluid at high Reynolds and moderate Weber numbers,” *J. Fluid Mech.* **307**, 191 (1996).
- ⁴⁶K. J. Chu and A. E. Duckler, “Statistical characteristics of thin wavy films: Part II. Studies of substrate and its wave structure,” *AIChE J.* **20**, 695 (1974).
- ⁴⁷K. J. Chu and A. E. Duckler, “Statistical characteristics of thin wavy films: Part III. Structure of the large waves and their resistance to gas flow,” *AIChE J.* **21**, 583 (1975).
- ⁴⁸H. Takahama and S. Kato, “Longitudinal flow characteristics of vertically falling liquid films without concurrent gas flow,” *Int. J. Multiphase Flow* **6**, 203 (1980).
- ⁴⁹L. Q. Yu, F. K. Wasden, A. E. Duckler, and V. Balakotaiah, “Nonlinear evolution of waves on falling films at high Reynolds numbers,” *Phys. Fluids* **7**, 1886 (1995).
- ⁵⁰T. B. Benjamin, “Wave formation in laminar flow down an inclined plane,” *J. Fluid Mech.* **2**, 554 (1957).

- ⁵¹C. S. Yih, "Stability of liquid flow down an inclined plane," *Phys. Fluids* **6**, 321 (1963).
- ⁵²J. Liu and J. P. Gollub, "Onset of spatially chaotic waves on falling films," *Phys. Rev. Lett.* **70**, 2289 (1993).
- ⁵³L. O. Jones and S. Whitaker, "An experimental study of falling liquid films," *AIChE J.* **12**, 525 (1966).
- ⁵⁴F. P. Stainthorp and J. M. Allen, "The development of ripples on the surface of liquid film flowing inside a vertical tube," *Trans. Am. Inst. Chem. Eng.* **43**, 85 (1965).
- ⁵⁵W. J. Strobel and S. Whitaker, "The effect of surfactants on the flow characteristics of falling liquid films," *AIChE J.* **15**, 527 (1969).
- ⁵⁶W. B. Krantz and S. L. Goren, "Stability of thin liquid films flowing down a plane," *Ind. Eng. Chem. Fundam.* **10**, 91 (1971).
- ⁵⁷F. W. Pierson and S. Whitaker, "Some theoretical and experimental observations of the wave structure of falling films," *Ind. Eng. Chem. Fundam.* **16**, 401 (1977).
- ⁵⁸G. J. Zabarar, "Studies of vertical annular gas-liquid flow," Ph.D. thesis, University of Houston, 1985.
- ⁵⁹J. Liu and J. P. Gollub, "Solitary wave dynamics of film flows," *Phys. Fluids* **6**, 1702 (1994).
- ⁶⁰P. Bach and J. Villadsen, "Simulation of the vertical flow of a thin, wavy film using a finite-element method," *Int. J. Heat Mass Transfer* **27**, 815 (1984).
- ⁶¹H. S. Khashgi and L. E. Scriven, "Distributed film flow on a vertical plane," *Phys. Fluids* **30**, 990 (1987).
- ⁶²T. R. Salamon, R. C. Armstrong, and R. A. Brown, "Traveling waves on vertical films: Numerical analysis using the finite element method," *Phys. Fluids* **6**, 2202 (1994).
- ⁶³L. W. Ho and T. Patera, "A Legendre spectral element method for simulation of unsteady incompressible viscous free-surface flows," *Comput. Methods Appl. Mech. Eng.* **80**, 355 (1990).

Physics of Fluids is copyrighted by the American Institute of Physics (AIP).
Redistribution of journal material is subject to the AIP online journal license and/or AIP
copyright. For more information, see <http://ojps.aip.org/phf/phfcr.jsp>
Copyright of Physics of Fluids is the property of American Institute of Physics and its
content may not be copied or emailed to multiple sites or posted to a listserv without
the copyright holder's express written permission. However, users may print,
download, or email articles for individual use.